Winter 2019

INVESTIGATION OF THE ACCURACY OF FINITE ELEMENT MODEL PREDICTIONS OF INTRINSIC RESIDUAL STRESS IN 3D WOVEN COMPOSITES BY COMPARING THE MODEL PREDICTIONS OF SURFACE DISPLACEMENTS FROM HOLE DRILLING TO EXPERIMENTAL MEASUREMENTS

Hilary A. Buntrock
University of New Hampshire, Durham

INVESTIGATION OF THE ACCURACY OF FINITE ELEMENT MODEL PREDICTIONS OF INTRINSIC RESIDUAL STRESS IN 3D WOVEN COMPOSITES BY COMPARING THE MODEL PREDICTIONS OF SURFACE DISPLACEMENTS FROM HOLE DRILLING TO EXPERIMENTAL MEASUREMENTS

BY

HILARY BUNTROCK

Bachelor of Science, University of Maine, 2016

THESIS

Submitted to the University of New Hampshire

in Partial Fulfillment of

the Requirements for the Degree of

Master of Science

In

Mechanical Engineering

December, 2019

This Thesis has been examined and approved in partial fulfilment of the requirements for the degree of Masters in Mechanical Engineering by:

Thesis Director, Dr. Todd S. Gross
Professor of Mechanical Engineering

Dr. Igor Tsukrov
Professor of Mechanical Engineering

Dr. Nikhil Padhye
Assistant Professor of Mechanical Engineering

On 12/9/2019

Original approval signatures are on file with the University of New Hampshire Graduate School.

Acknowledgements

Table of Contents

List of Tables

List of Figures

ABSTRACT

INVESTIGATION OF THE ACCURACY OF FINITE ELEMENT MODEL PREDICTIONS OF INTRINSIC RESIDUAL STRESS IN 3D WOVEN COMPOSITES BY COMPARING THE MODEL PREDICTIONS OF SURFACE DISPLACEMENTS FROM HOLE DRILLING TO EXPERIMENTAL MEASUREMENTS

By
Hilary Buntrock
University of New Hampshire

The goal of this effort was to determine how accurately finite element models of 3D woven composites constructed using Dynamic Fabric Mechanics Analyzer predict the intrinsic residual stress field that results from cooling going from the curing temperature to room temperature. Hole drilling methods were used to estimate and measure the local stresses at selected locations in 3D woven composites. Blind holes were virtually drilled in one orthogonal and multiple ply-to-ply models and the resulting in-plane surface displacement fields were compared to the surface displacement fields measured using electronic speckle pattern interferometry.

The shape of the experimental and predicted displacement fields were similar in both the orthogonal and ply-to-ply structures, except along the orthogonal warp tow, where the fields were opposite. The magnitude of the measured displacement fields was approximately $1/5^{th}$ that of the predicted value both parallel and perpendicular to the tows in the orthogonal structure, except along the orthogonal warp tow, which was $-1/5^{th}$. This is attributed to microcracking below the warp tow relieving the residual stress. The magnitude of the experimental

x

displacements was between $1/3^{rd}$ to two times larger than the prediction transverse to the tow axis in the ply-to-ply structure. Along the warp tow axis, on one side the experimental result matches the prediction while on the other side the experimental displacement was two times larger. Along the weft tow in the ply-to-ply the experimental displacement matched the predicted displacement.

The effect of drill depth on surface displacement was studied by drilling holes in 0.5mm depth increments and comparing experimental results to finite element models of an orthogonal and a 12x10 picks per inch ply-to-ply structure. The experimental displacements match the predicted displacements in shape and magnitude. The model does a good job of predicting the effect of drill depth on surface displacement.

The effect of pick spacing and volume fraction on surface displacements from hole drilling was studied for composites with a ply-to-ply weave with 12x12 (warp/weft) picks per inch (ppi), 10x12 ppi, and 10x8 ppi. The finite element models used in this section contained a resin overburden on top of the tows, affecting the accuracy of the predicted displacements. The experimental displacement fields were a good qualitative match to the predictions. The experimental transverse displacements were approximately 1/4 of the predicted displacements. The model increasingly under predicts the displacement along the tow axis as the number of picks-per-inch decreases.

Chapter 1: Introduction

Composite materials have been used since biblical times, in things like straw reinforced bricks [1] or plant fiber reinforced pottery [2]. Today composites are much more advanced and used in a wider range of applications such as pipes, boats, cars, or sports equipment. Modern composites can be developed with specific material properties, and are lighter and stronger than traditional metal components, which is why 50% of the Boeing 787 Dreamliner and 53% of Airbus A350 XWB are now made out of carbon fiber reinforcement polymer composites (CFRP). In the automotive industry, switching to composites can make the cars lighter by 30%, greatly increasing fuel efficiency and speed of the car.

The drawback to CFRPs produced by laminating layers of glass or carbon fiber cloth is the potential for delamination. One approach to prevent this is 3D woven carbon fiber used to interlock the layers together. This makes the composite more resistant to delamination, increases fatigue resistance, and enhances the through-the-thickness thermal conductivity. However, the through-the-thickness constraint introduces triaxial residual tensile stress in the resin pockets during the cool down cycle that can lead to microcracking.

This work discusses the methods used to estimate the intrinsic residual stress field in several woven composite architectures by comparing experimentally-measured surface displacement fields induced by hole drilling to the fields estimated from virtual hole drilling in a finite element model of the composite. The surface displacement was measured using electron speckle pattern interferometry (ESPI). The finite element model utilizes temperature dependent resin properties

for the matrix and temperature independent, transversely isotropic properties for the fiber tows. The physical location of the tows was defined using Dynamic Fabric Mechanical Analyzer software (DFMA) ([3], [4]).

The experimental response is compared to prediction for a ply-to-ply weave with no expected through-the-thickness constraint and an orthogonal weave with high through-the-thickness constraint. The impact of weave density in the ply-to-ply structure on the surface displacement fields from hole drilling is also presented. The last study compares experimental and predicted results for holes drilled in the same location in the ply-to-ply and orthogonal structures at 0.5mm depth increments.

Chapter 2: Background

2.1 Fiber-reinforced Polymers

Fiber-reinforced polymer (FRP) composites are made by combining a polymer resin with reinforcing fibers. This type of material is very popular because, through selection of the resin and fiber materials, the properties of the composite can be carefully tailored for a specific application. FRP composites can be made to have the same properties as, for example, an aluminum airplane wing panel, and can replace that part with the same performance but weigh only 60% as much [5].

The fibers commonly used are made of carbon, graphite, aramid, or glass, depending on the desired properties and uses. The primary purpose of the fibers is to provide strength and stiffness. The matrix is used to bind the reinforcement together, provide shape and structure, and protect the reinforcements from mechanical or environmental damage. The matrix is most commonly made of polymer thermosets due to their strong cross-linked structure formed during the cure cycle [5].

2.2 Cure cycle

Epoxies are formed using a cure cycle with temperature stages to control the crosslinking process. During the cure cycle the epoxies transform from a liquid to a glassy solid with a cross-linked molecular structure. A fully-cured epoxy forms a dense network with only a few linking units between network points. This dense network of links provides properties such as a high glass transition temperature, low shrinkage, high adhesive strength, chemical resistance, and heat resistance.
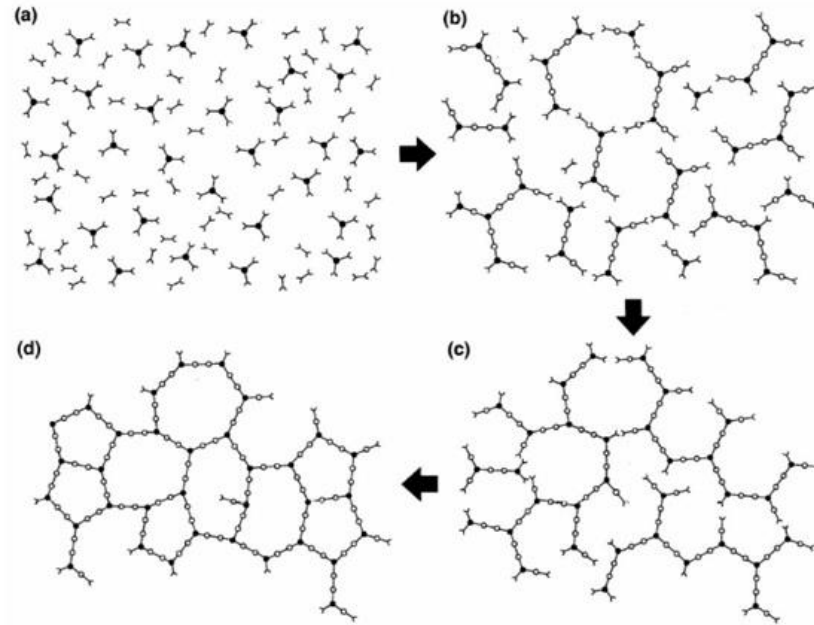
Figure 1: Progress of cure in an epoxy resin,(a) liquid state, (b)cross-linking begins, (c) gelation caused by further crosslinking, (d) fully cured resin network [6]

Many polymer matrix composites have a two-step cure cycle like the one in Figure 2 to ensure a complete cure of the resin. The composite is heated up to the 1st dwell temperature and held there with a vacuum applied to allow entrapped gasses to escape the matrix and for the resin to flow throughout the fiber weave. Then, the temperature is increased to the second dwell and held for the duration of the curing cycle. This dwell is when the resin components crosslink as seen in Figure 1 (c), and based on the dwell time and temperature, the composite properties can be controlled. Finally, the part is cooled down to room temperature at a constant rate. The second dwell needs to be above a certain minimum temperature to complete the cross-linking, so, too low of a temperature can lead to an incomplete cure [[7]; [8]].
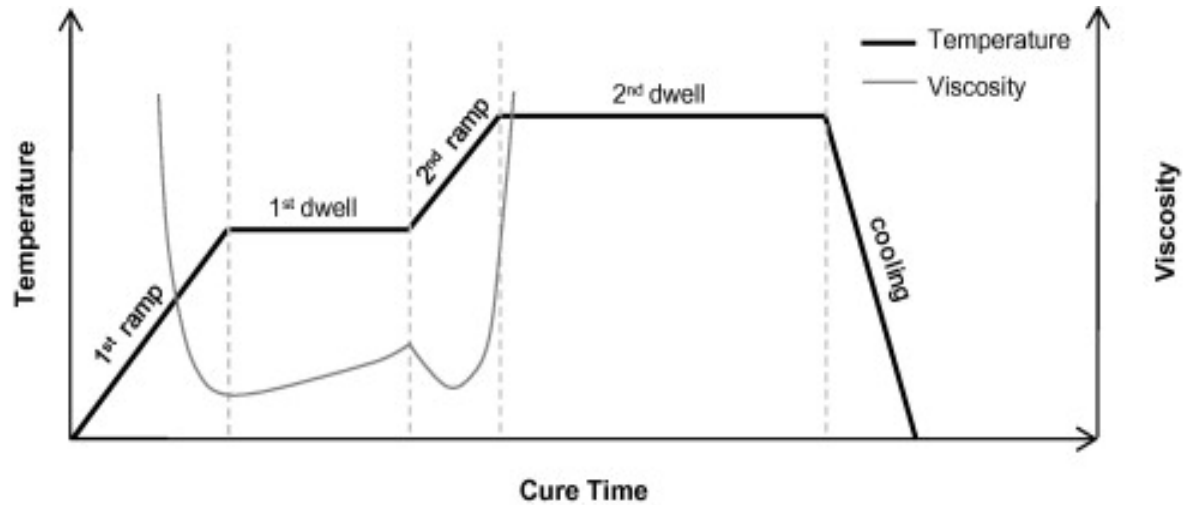
Figure 2: Two-step cure cycle [9]

At the end of the high cure temperature of the 2nd dwell, the epoxy composite is in a zero stress

state. As the composite cools down, the resin and the fiber contract at different rates due to a

difference in coefficients of thermal expansion (CTE) leading to an intrinsic residual stress field

at room temperature. The fibers used this this work have a transverse to the fiber axis CTE of

6×10^{-6} (/°C) and a longitudinal to the fiber axis CTE of -4×10^{-7}(/°C) while the resin CTE is 5-

7.5×10^{-5}(/°C) [10].
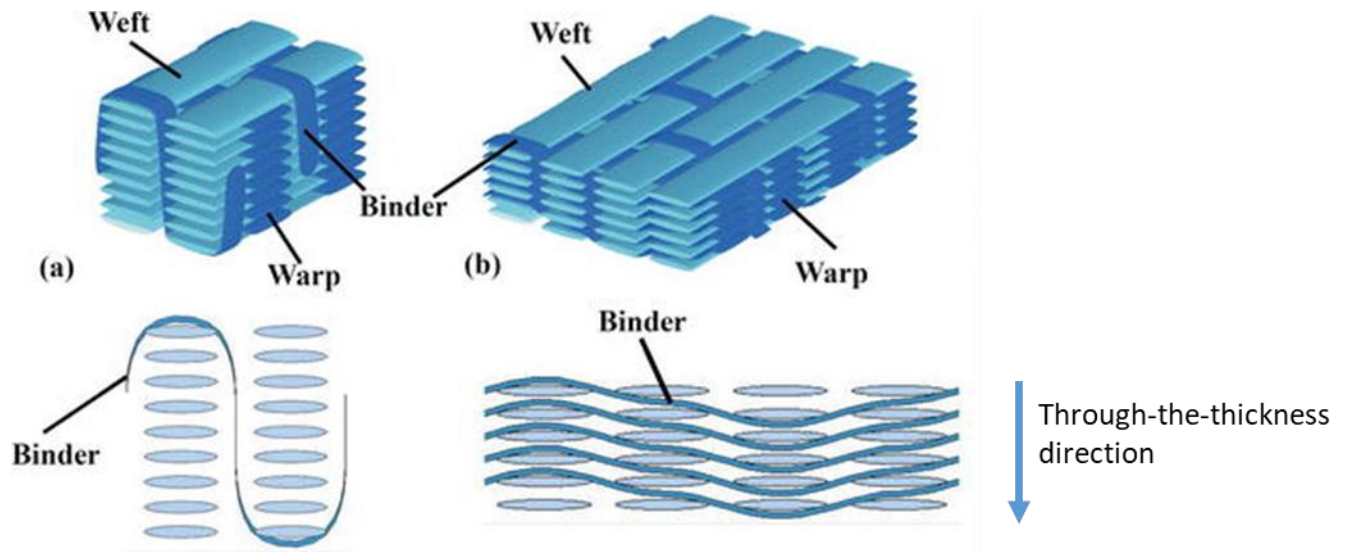
Figure 3: Diagram of orthogonal and ply-to-ply weaves with terms explained. (a) Standard orthogonal weave in isometric view and side view looking down the weft fibers. (b) Standard ply-to-ply weave in isometric view and side view looking down the weft fibers. For the extent of this paper binder tows are referred to as warp tows. [11]

3D woven composites with a high degree of through-the-thickness constraint exhibit matrix micro-cracking [12] in the resin pockets. The cracks are attributed to the hydrostatic tensile stress in the resin pockets [12] caused by the differences of CTE between the carbon fibers and the epoxy matrix.
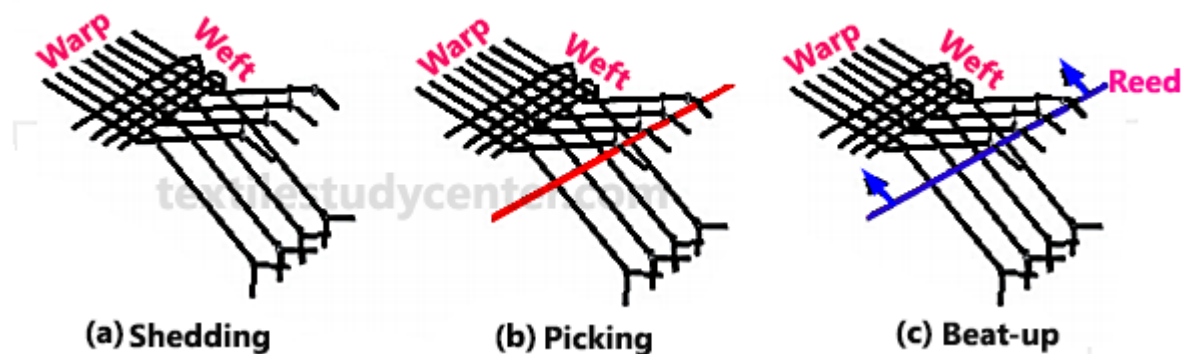
Figure 4: The primary motions of a loom. (a) diving the warp yarns into two groups to allow passage of the weft yarn. (b) transferring the weft yarn from one side of the loom to the other. (c) pushing the weft yarn into the pattern [13].

Weaving a composite fabric is done in the three primary motions shown in Figure 4. Shedding is when the warp is divided into groups so they can be separated and the weft yarn can be run between them. Picking is transferring the weft yarn from one side to the other. Beat up is pushing the newly inserted weft yarn into the its place [13]. In Figure 3 it is shown how weft yarns are kept straight (the light blue) while the warp yarns (in dark blue) bend around them.

Chapter 3: Materials and methods

3.1 Samples from Albany

Panels of 4.1 mm thickness were fabricated by Albany Engineered Composites using Hexcel RTM6 resin and Hexcel 12K IM7 PAN-based carbon fiber tows. The ply-to-ply architecture has an in-plane unit cell dimensions of 10.16 mm by 8.47 mm. The orthogonal architecture has an in-plane unit cell dimensions of 5.1 mm by 5.1 mm and represents the maximum through-the-thickness constraint for this work. A unit cell is the smallest repeated portion of the material possessing the same mechanical properties as the entire material

For the alternate weave study, all panels had the ply-to-ply architecture (shown in Figure 5) and had in-plane unit cell dimensions of 10.16 mm by 10.16 mm. Each panel had different overall volume fraction of fiber and different number of warp and weft picks-per-inch (ppi). The details of each panel are summarized in Table 1.

Table 1: Volume fraction of considered woven architectures [14].

Architecture	$V_{f\text{-warp}}$	$V_{f\text{-weft}}$	V_f
Ply-to-ply (12x10 picks-per-inch)	0.36	0.33	0.69
Orthogonal	0.36	0.33	0.69
12 x 12 picks-per-inch	0.37	0.39	0.76
10 x 12 picks-per-inch	0.31	0.39	0.70
10 x 8 picks-per-inch	0.30	0.26	0.56
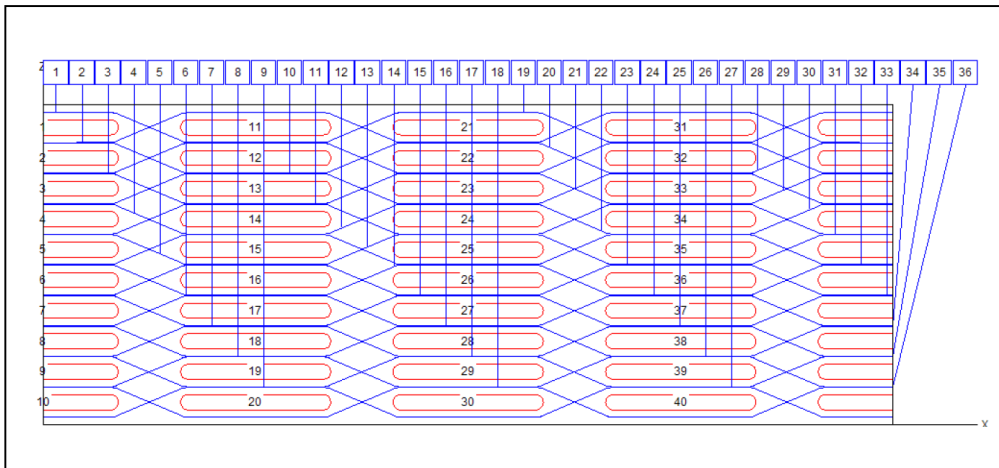
Figure 5: Schematic of ply-to-ply weave looking in the weft direction. The red ovals represent the weft fibers and the horizontal blue lines are the warp fibers.

3.2 Electronic Speckle Pattern Interferometry

The surface displacements are tracked using a custom built electronic speckle pattern interferometry (ESPI) system similar to the one described in [15]. Two beams from a linearly polarized 50 mW Melles-Griot He-Ne laser beam illuminate the sample surface at a $\theta = \pm 45°$ angle to the surface normal. This arrangement is only sensitive to displacements in the plane of the two beams.

The displacement is calculated using *before* and *after* images of the sample. The two light beams interact to create a speckle light pattern and four before-images are taken where the piezoelectric translator shifts the path length of one of the beams so that the optical phase smoothly changes by $\pi/2$ during each image acquisition period. The four obtained images of the intensity, I, are combined to solve for a modulo 2π optical phase map, $\phi(x, y)$, using the following equations:

$$I = \int_0^{\pi/2} I_o \left(1 + m\cos(\phi + \delta)\right) d\delta \qquad I_1 = \int_{\pi/2}^{\pi} I_o \left(1 + m\cos(\phi + \delta)\right) d\delta$$

$$I_2 = \int_{\pi}^{3\pi/2} I_o \left(1 + m\cos(\phi + \delta)\right) d\delta \qquad I_3 = \int_{3\pi/2}^{2\pi} I_o \left(1 + m\cos(\phi + \delta)\right) d\delta \qquad (1)$$

$$\phi(x, y) = \tan^{-1}\left[\frac{I_3 - I + I_2 - I_1}{I - I_1 + I_3 - I_2}\right]$$

where m is the amplitude of the intensity modulation, I_o is the average intensity, and δ is the applied phase shift, and $\phi(x, y)$ is the modulo 2π optical phase being solved at each pixel. The same process is repeated after the hole drilling to create another modulo 2π optical phase map. The after-phase map is subtracted from the before phase map to create a phase difference map. These phase maps must be unwrapped to get the total phase difference which may be more than $\pm\pi$. We used

a program from Matlab Central (https://www.mathworks.com/matlabcentral/fileexchange/60345-2d-weighted-phase-unwrapping) based on the algorithm of [16] to unwrap our phase maps.

The phase difference map is converted to displacement using the equation.

$$u(x, y) = \frac{\phi(x, y)\lambda}{4\pi \sin \theta} \tag{1}$$

where laser wavelength $\lambda = 632.8$ nm, $\theta = \pm 45°$, and ϕ is the phase difference. Figure 6 shows a modulo 2π optical phase map where the optical phase is encoded as black for $\phi = -\pi$ and white for $\phi = \pi$. The phase difference determination noise was determined by computing the average and standard deviation of an area of greater than 1000 pixels for which there was no change between the before and after image. The noise is $<\pi/25$ which corresponds to a displacement of 9 nm.

There is a region adjacent to the hole edge where the before and after image are either not correlated or the fringe density is too great to unwrap. A good portion of the decorrelated region is caused by the surface changing so much that it generates a speckle pattern that has no relation to the first image. Figure 6 shows an example of both decorrelation around the hole, indicated by the red circle around the hole, and high fringe density (on the right side of the hole). This region is somewhere between 0.14 and 0.2 mm from the edge of the 1 mm diameter hole (shown by the white circle) and is excluded from our results.

11
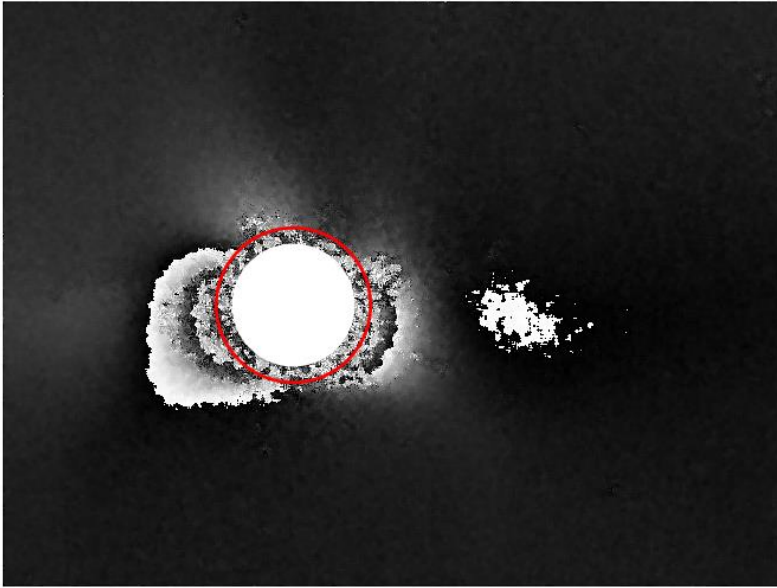
Figure 6: Modulo 2π phase map where a phase of $-\pi$ is encoded as black and π is encoded as white. The red line shows the region that is excluded from our experimental data due to possible surface changes and high fringe density.

3.3 Sample preparation and hole drilling (paint, cutting, gluing)

The composite samples were cut down to sections containing at least nine unit cells and prepared for drilling by using a x-y translating mount and a microscope with crosshairs to locate the coordinates of the desired hole location. Then, the sample was spray painted with white, high heat paint, airbrushed with fine black speckles, followed by a clear matte surface coat. The white paint causes the laser illumination to diffusely reflect from the surface toward the camera. The black speckles make the intensity more uniform. The clear surface coat protects the white paint from the effects of the cooling water during drilling and also prevents debris from sticking to the surface. When the coatings were dry, the sample was placed back on the translator mount and the crosshairs was used to locate the desired hole. A fine point black sharpie was used to place a dot over the drilling location. The imprecision of this method sometimes resulted in small deviations from the intended drilling location. The sample was then glued onto a kinematic mount that allows for exact sample placement before and after drilling, and can precisely rotate by 90° to capture horizontal and vertical displacements about the hole.

The sample was drilled using a UKAM 1 mm diameter diamond coring tool. The hole was drilled using a SERVO precision drill press which can accurately control hole depth to 0.01mm using a dial indicator depth stop. A drop of deionized water was manually applied to the area to be drilled to suspend the drilling debris. After drilling, the sample was rinsed with deionized water and dried with filtered air.

3.4 Finite Element Analysis

The finite element models utilized in this work were constructed and executed by Kostia Vasylevskyi as part of his Ph.D. research. The following sections summarize the model details and some of the key results.

3.4.1 Finite element background

A realistic geometric model of the weave architectures was constructed using Dynamic Fabric Mechanical Analyzer (DFMA) (see [3]; [4]). This software models digital fibers as digital rod elements connected with flexible links and contact elements. The digital fibers are combined into yarns where all fibers have the same length. The volume occupied by one digital fiber would be filled by multiple actual fibers. One can then specify the number of digital fibers per yarn and whether the fibers in the yarn are straight or twisted. The yarns are assembled into an expanded representation of the unit cell topology and the final unit cell is determined from a dynamic relaxation approach. The cross-sectional profiles of each yarn in the final structure are exported as a point clouds used in surface reconstruction algorithms to create the finite element mesh of the unit cell using a custom Matlab script. Some yarns do not reach the unit cell boundary due to yarn end caps not running parallel to the boundary, so yarn periodicity conditions are implemented to allow the yarn to extend beyond the unit cell [17]. Later excessive yarn elements are cut off to form flat unit cell surfaces. All model preparation steps are performed automatically within the MSC Mentat software using a custom Python script and at the completion of the script the user is presented with a ready-to-run model.

The volumetric mesh for the tows is generated using Marc Mentat based on the surface mesh for the yarns in the unit cell. To better control the mesh, the yarn profiles are re-discretized through

14

interpolation to create a more refined point profile. The level of discretization in the longitudinal yarn direction is controlled by selecting the number of cross-sectional profiles using in the FE mesh generation. The volumetric mesh for the resin is generated in Marc Mentat by changing the sign of the normal vector to the surface mesh of the yarn. Custom scripts are used to improve the surface mesh at the lateral boundaries of the unit cell so that the mesh of the unit cell is rigorously/exactly congruent (nodal pattern is the same). More details of this process can be found in [18]. In the 12x12, 10x12, and 10x8 picks-per-inch models there are areas of penetration between adjacent tows that are corrected manually and using custom scripts. The script identifies the nodes of a tow inside another tow and moves them in the direction of the mean normal of all penetrating surface elements until the interpenetration is removed. This produces the FE mesh of the reinforcement geometry for analysis with minimal disturbance to the tow geometry [12]. This results in differences between the model and the tow volume fraction used to fabricate the specimens. This difference is greatest for the 10 x 12 architecture.

The properties of the RTM6 epoxy matrix are assumed to be homogeneous and isotropic. The Young's modulus, E, and coefficient of thermal expansion, α, depend on temperature as:

$$E_m = E_m^{0^o C} - \beta_m T$$
$$\alpha_m = \alpha_m^{0^o C} + \gamma T$$

(3)

where $E_m^{0°C} = 350 MPa, \beta_m = 5.9 \frac{MPa}{°C}, \alpha_m^{0°C} = 5*10^{-5} \frac{1}{°C}, \gamma_m = 1.05*10^{-7} \frac{1}{°C}$, and T is in °C.

The yarns are modeled as a transversely isotropic material that represents the resin impregnated 12K carbon fibers assuming an 80% volume fraction of fibers within the yarns. The effective properties are estimated using micromechanical models of Hashin and Shapery ([19]; [20]) for continuous unidirectional composites as E_{1t} = 221.38 GPa, E_{2t} = 13.18 GPa, G_{12t} = 7.17 GPa, v_{12t} = 0.35, v_{23t} = 0.35, α_{1t} = −2.29·10− 7 K^{-1}, α_{2t} = 2.23·10^{-5} K^{-1}. In these expressions, direction 1 is parallel

to the axis of the yarn and directions 2 and 3 are transverse to the yarn axis. Note that even though the properties of the matrix in the tows change with temperature as given by (3), these changes will result in insignificant variations of the homogenized properties of the tows (see comparison in [12]), so in the numerical simulations the properties of the tows are assumed to be temperature independent.

The hole drilling was simulated using Marc Mentat's capability to deactivate elements. First, the simulation of the cooling after curing was performed assuming that the temperature of the completely cured composite panel uniformly changes from 185°C to 25°C while lateral surfaces of a unit cell stay periodic but are allowed to move laterally to accommodate the overall shrinkage of the composite panel. Then, the elements corresponding to the position of the hole were manually selected to deactivate. Subtracting the displacements obtained after the simulation of curing from the displacements after removing the elements representing the hole produces the displacement field from the hole drilling.

3.4.2 Finite element predictions of stress fields

The predicted values of in-plane stress in the tows for the orthogonal structure is shown in Figure 7. The stress models in Figure 7, Figure 8, and Figure 9 are one unit cell, which is the smallest repeated portion of the material possessing the same mechanical properties as the entire material. The warp direction is the "1" or "x" direction. The side-by side plots show the color bar for tensile stresses on the left and for the compressive stresses on the right. The compressive stress area is gray on the left and the tensile stress area is gray on the right. The stresses transverse to the tows are tensile and the longitudinal stresses are compressive. The stresses in the resin, seen in Figure 9, are nearly triaxial tensile and in the range of 40-60 MPa (each component and the hydrostatic

16

tensile stress). The stresses presented in this section are calculated based on models that have an overburden of epoxy on top of the tows. A discussion of how the overburden affects surface displacement during hole drilling is presented in section 4.3 of this paper. The overburden is not expected to significantly impact the predicted internal stress fields.
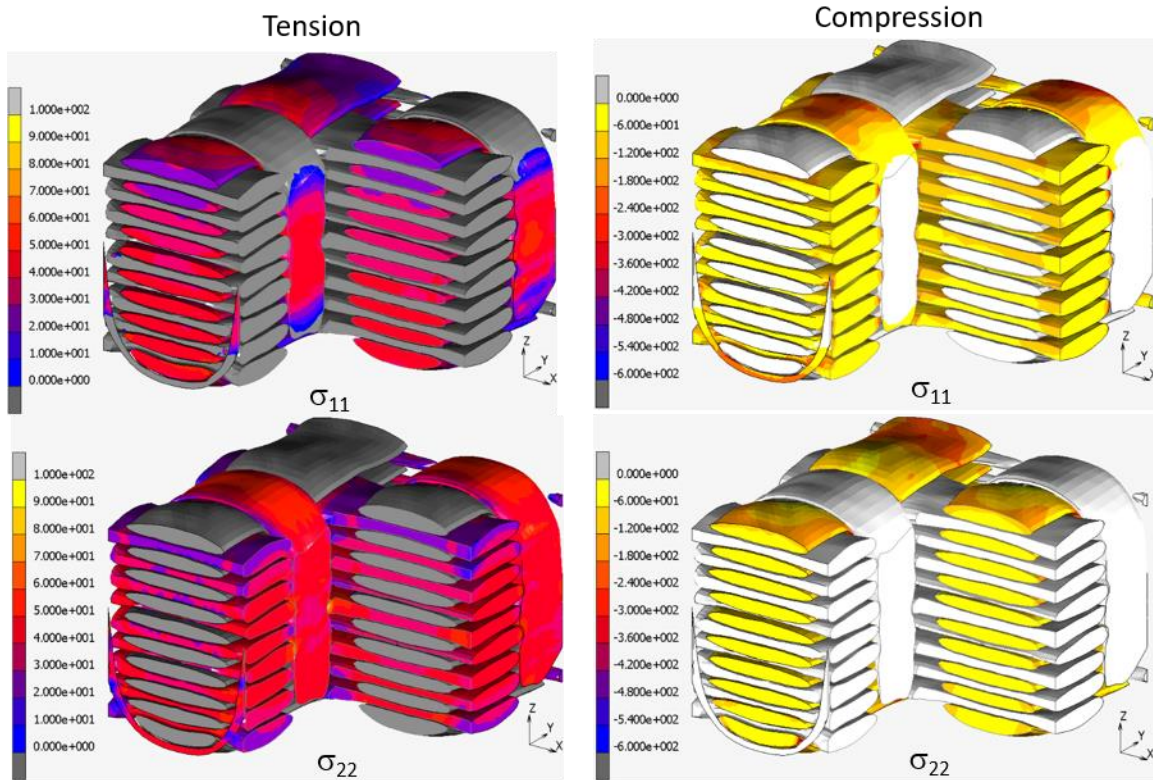
Figure 7: In-plane stresses in orthogonal structure. Note that all stresses along the axis of the tows are compressive and all stresses transverse to the tows are in tension. Stresses are in MPa. Stress models created by Kostiantyn Vasylevskyi at University of New Hampshire.

The in-plane stress components in the tows for the ply-to-ply structure are shown in Figure 8. Again, all the transverse stresses are tensile and the longitudinal stresses are compressive. The stresses in the resin are also nearly triaxial tensile and are in the range of 40-60 MPa as seen in Figure 9. This is the same as for the orthogonal although the maximum stresses are 30-50 MPa for ply-to-ply and are 60-70 MPa for the orthogonal.
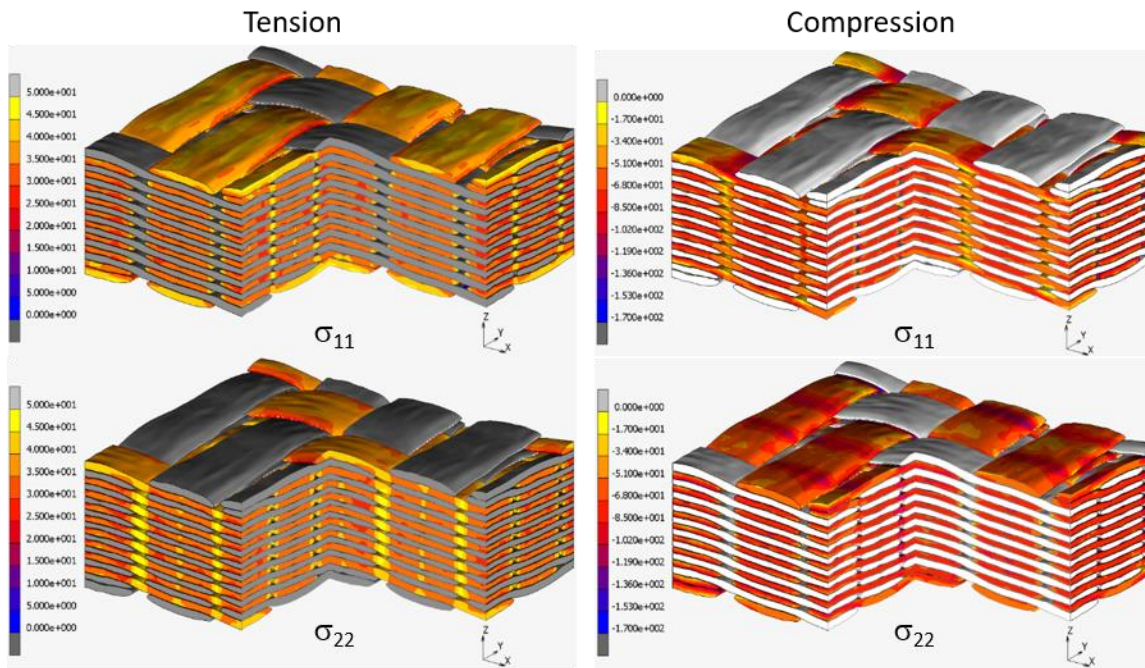
Figure 8: In-plane stresses in ply-to-ply structure. Note that all stresses along the axis of the tows are compressive and all stresses transverse to the tows are in tension. Stresses are in MPa. Stress models created by Kostiantyn Vasylevskyi at University of New Hampshire.
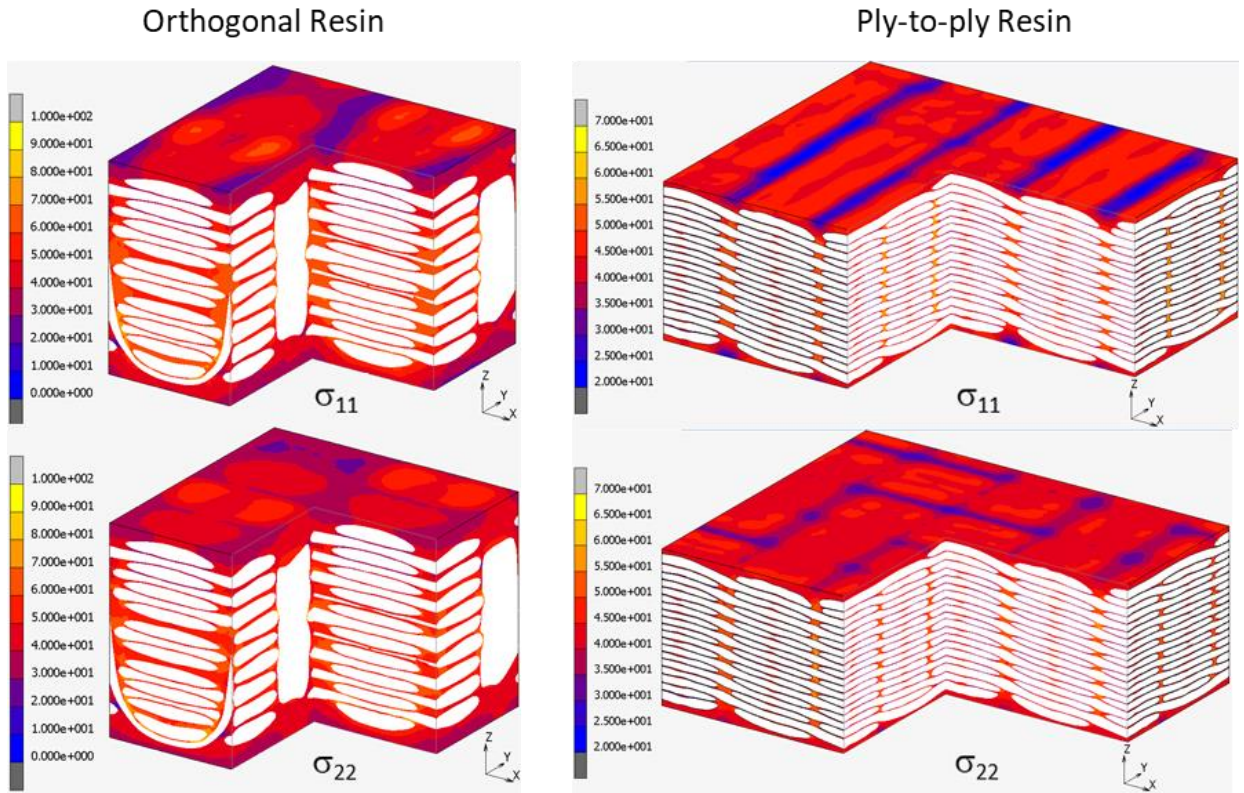
Figure 9: In-plane stresses in orthogonal and ply-to-ply resins. Note that all stresses are tension. Stresses are in MPa. Stress models created by Kostiantyn Vasylevskyi at University of New Hampshire.

The magnitude range of the stresses is summarized in Table 2. The transverse stresses are similar in all tows and architectures. The magnitude of the warp and weft longitudinal stresses in the ply-to-ply are the same. The warp longitudinal stress in the orthogonal structure is larger than the weft longitudinal stress, and both are larger than the ply-to-ply longitudinal stresses. The orthogonal stresses also have a larger range of magnitude than the ply-to-ply stresses.

Table 2: Predicted in plane stresses for tows in orthogonal and ply-to-ply structures

Orthogonal		Minimum (MPa)	Median (MPa)	Maximum (MPa)
Warp	longitudinal	-162	-99	-37
	transverse	20.4	33	56
Weft	longitudinal	-152	-87	-33
	transverse	17	32	67
Resin	All directions	22	55	75
Ply-to-ply				
Warp	longitudinal	-97	-71	-33
	transverse	27	31	46
Weft	longitudinal	-101	-73	-33
	transverse	26	31	45
Resin	All directions	20	42	50

When we virtually drill into the tows, we expect that the stress state in the tow will control the displacements. We expect to see outward transverse displacements in both structures because of the transverse tensile stress and inward longitudinal displacements because of the longitudinal compressive stresses. However, there are certain situations where the displacements very near (within 150 μm) to the edge of the virtual hole may be influenced by the resin layer resulting in the hole expanding (outward displacements) in regions where we expect the hole to contract (inward displacements).

Chapter 4: Results

The results are presented in three formats. First the displacement fields are qualitatively compared via surface displacement field plots. The red shades are positive displacement and the blue shades are negative displacement. These plots allow an analysis of the displacement field shape and intensity along and transverse to the fiber tow axis. Around the hole on these plots, is a black ring. For the predicted results this just highlights the drill location, but for the experimental results the thickness of this ring represents the decorrelation zone due to either drilling or a fringe density that is too high to resolve.

Second, the surface displacements are combined into a quiver plot with vectors of relative magnitude and direction of displacement. When overlaid on the weave image, this shows how specific fiber and resin regions react to the removal of material.

The third method of displacement comparison is slice plots along and transverse to the tow axis through the center of the hole. Comparing slices of displacement data allows a scale comparison of maximum displacement observed and another method to compare displacement field shape through the slope of the slice plots. Slices are always taken in the direction of maximum displacement, i.e. slices parallel to the tow axis show displacements parallel to the tow axis and slices perpendicular to the tow axis show displacements perpendicular to the tow axis. The experimental slice data is an average of 11 rows or columns parallel to the slice to reduce any random pixel errors from the data. This represents an approximately 100 μm width.

The results covered in this section are arranged according to the research question that defined the goal of each study. The overall objective is to evaluate the accuracy of the model predictions by comparison to the experimental measurements.

4.1 The ability of the finite element model to predict the surface displacement field was studied for both the orthogonal and a 12x10 ppi ply-to-ply architecture.

4.2 The effect of hole depth on the surface displacement field was studied for both the orthogonal and 12x10 ppi ply-to-ply architectures.

4.3 The effect of weave density on the surface displacement field in the ply-to-ply structure was studied.

4.1 Comparison of the finite element model to the experimental results

4.1.1 Ply-to-ply warp results

The results for the ply-to-ply warp tow are shown in Figure 10. The shape of the predicted and experimental displacement fields for the ply-to-ply warp tow transverse to the tow axis are a match. Close to the edge of the hole, the transverse experimental displacement matches the predicted displacement in scale, as seen in the slice plot in Figure 11. Further away from the hole the experimental displacement are two times larger than the predicted results. This change in scale also coincides with a displacement sign reversal and is coincident with the edge of the tow. Along the warp tow, the experimental displacement is similar in shape to the predicted displacement. The slice plot for the longitudinal results in Figure 11 show that on one side of the hole, the displacements are a scale match. On the other side of the hole, the experimental displacement is approximately two times larger than the predicted displacement.
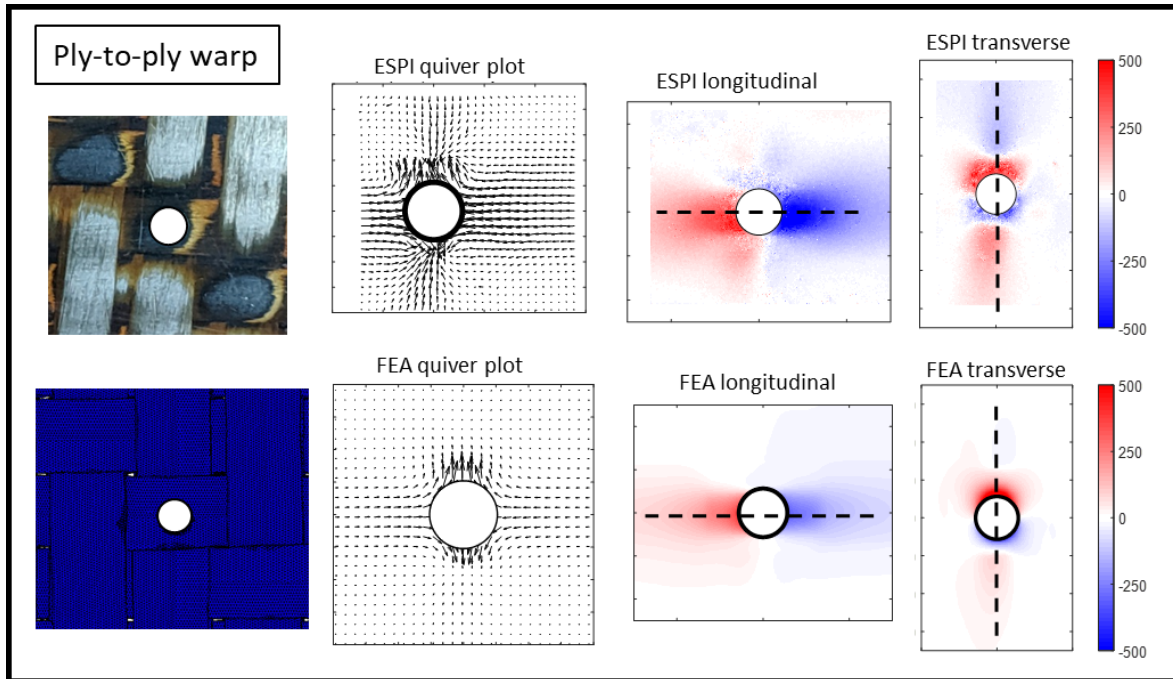
Figure 10: Displacement fields for 1 mm hole drilled in warp tow in ply-to-ply architecture. The top row shows the observed displacements and the bottom row shows the predicted displacements. The images on the left show the actual location of the hole and the location in the finite element mesh. The quiver plots show the combined x and y displacements. The dashed lines show the location of the slice plots in Figure 11.
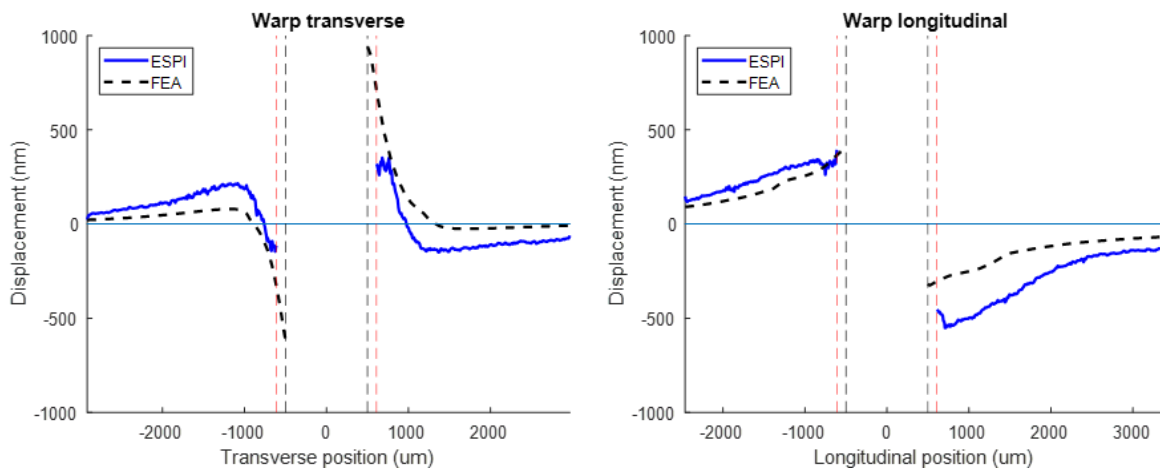
Figure 11: Slices through the displacement fields in Figure 10. The displacements parallel to the shows good agreement with the FEA prediction. The slice transverse to the tow shows a slight displacement scale difference with the FEA prediction.

4.1.2 Ply-to-ply weft results

Figure 12 shows the experimental and predicted results for a hole drilled in the middle of the ply-to-ply weft tow. The shape of the displacement fields is very similar transverse to the tow axis, however, the predicted displacement is larger than the experimental displacement. The displacements parallel to the tow axis are similar in shape and magnitude.
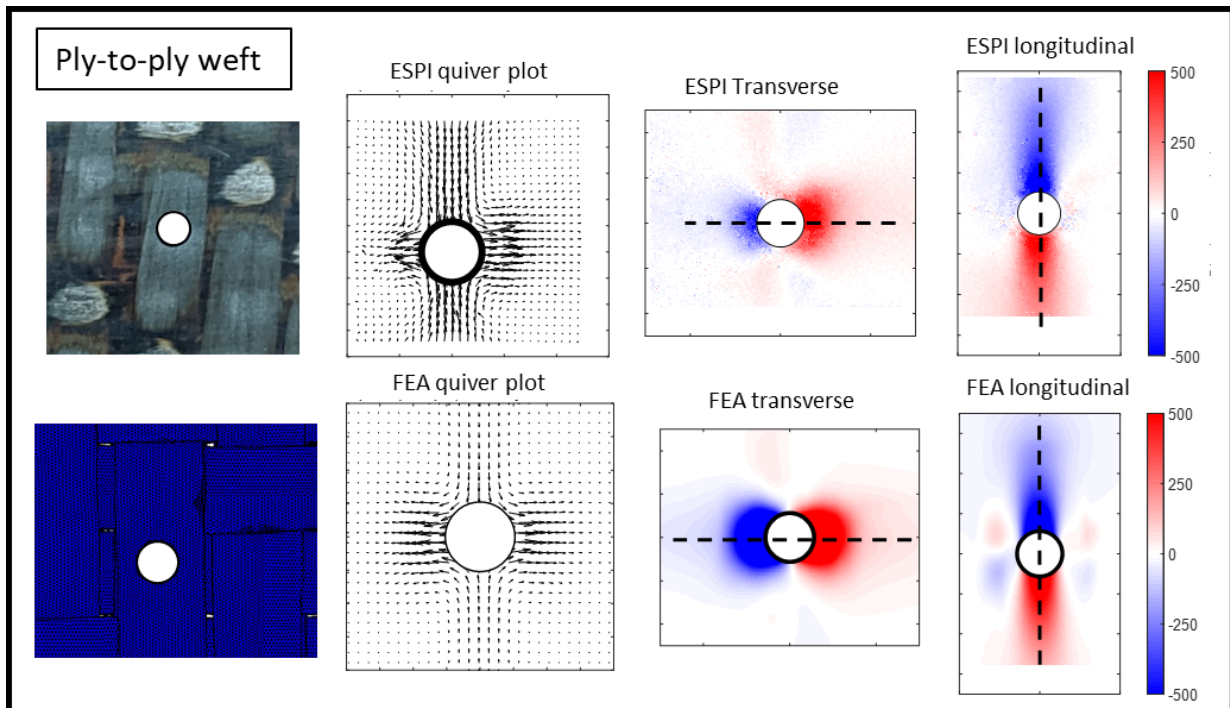
Figure 12: Displacement fields for hole in center of the weft tow in the ply-to-ply structure. The dashed lines show the positions of the slices in the subsequent figure. The dashed lines show the position of the slices in Figure 13.

Figure 13 shows the slice plots of the data represented by the dashed line through the ply-to-ply center weft displacement field plots in Figure 12. The transverse slice plot shows that the magnitude of experimental displacements close to the hole is approximately 1/3rd of the predicted displacements while further away from the hole the scale of the displacements is approximately the same. The longitudinal displacements exhibit a very good match between the experimental and predicted results

25
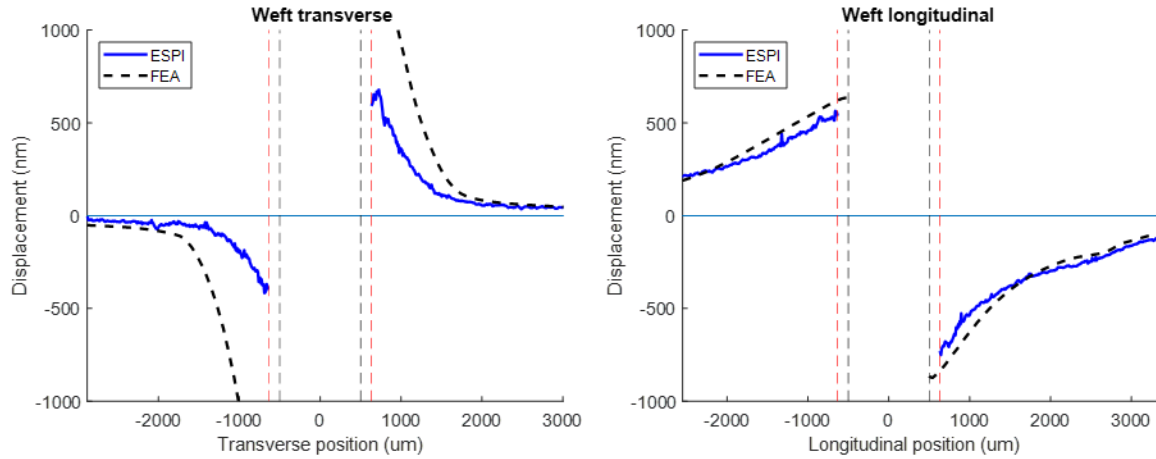
Figure 13: Slices through displacement fields shown in Figure 12. Left hand slice transverse to weft tow in ply-to-ply structure showing good agreement with 1/3rd the predicted FEA displacement. The right hand slice shows the displacements parallel to the tow axis and shows good agreement with the full FEA prediction.

4.1.3 Orthogonal warp results

The hole in the orthogonal warp tow in Figure 14 was drilled slightly off center of the tow. The model was adjusted to closely match the position of the actual hole. The transverse displacement fields are a very good match in shape. The hole shows an opening response close to the hole and closing further away. This change in displacement direction is coincident with the edge of the warp tow. The observed results along the tow axis show the hole opening. The predicted results show the hole closing. This conflicting response is attributed to microcracking in the resin relieving internal residual stress in the composite, an effect that is not represented in the FE model.

26
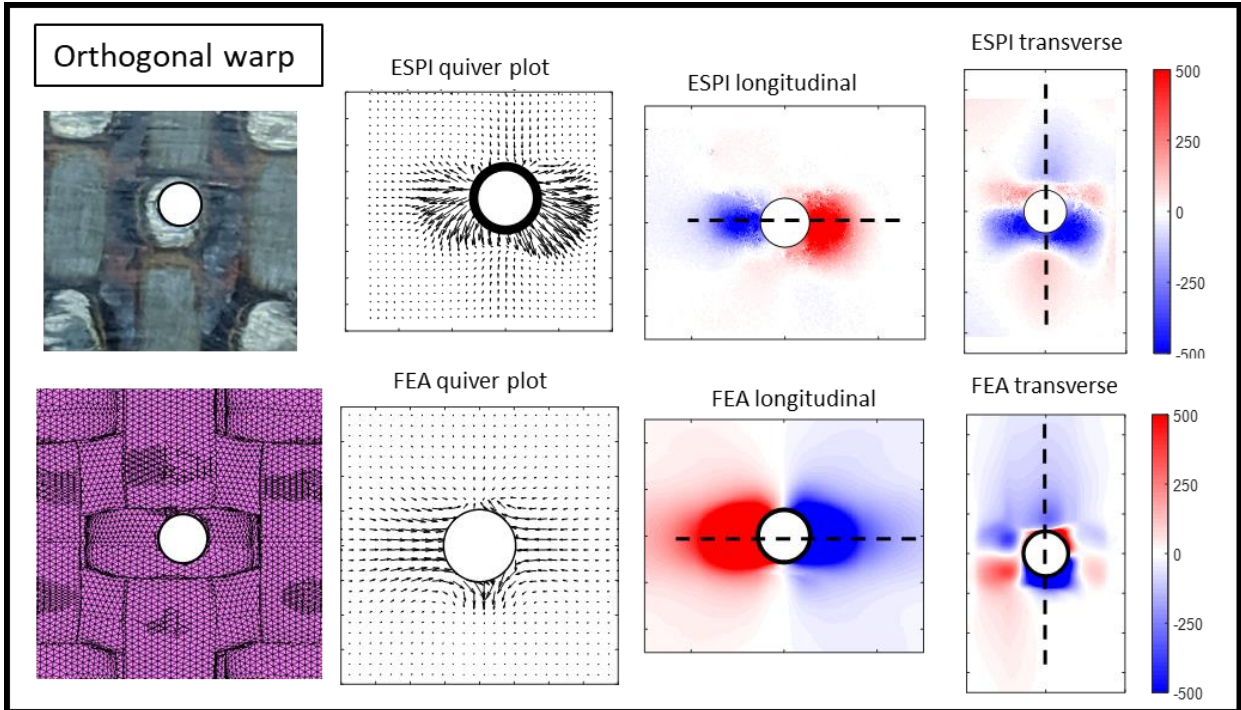
Figure 14: Observed (upper row) and predicted (lower row) displacement fields resulting from a hole drilled slightly off center in a warp tow in the orthogonal structure. The dashed lines show the location and direction of the slice plots in Figure 15.

The slice plots in Figure 15 show the experimental displacements transverse to the orthogonal warp tow are $1/3^{rd}$ to $^1/5^{th}$ of the predicted displacements. Note that both slice plots use $1/5^{th}$ of the predicted value. The longitudinal slice plot shows that the observed displacement is opposite of the predicted displacement, and the experimental results are approximately $1/5^{th}$ the magnitude of the predicted results.
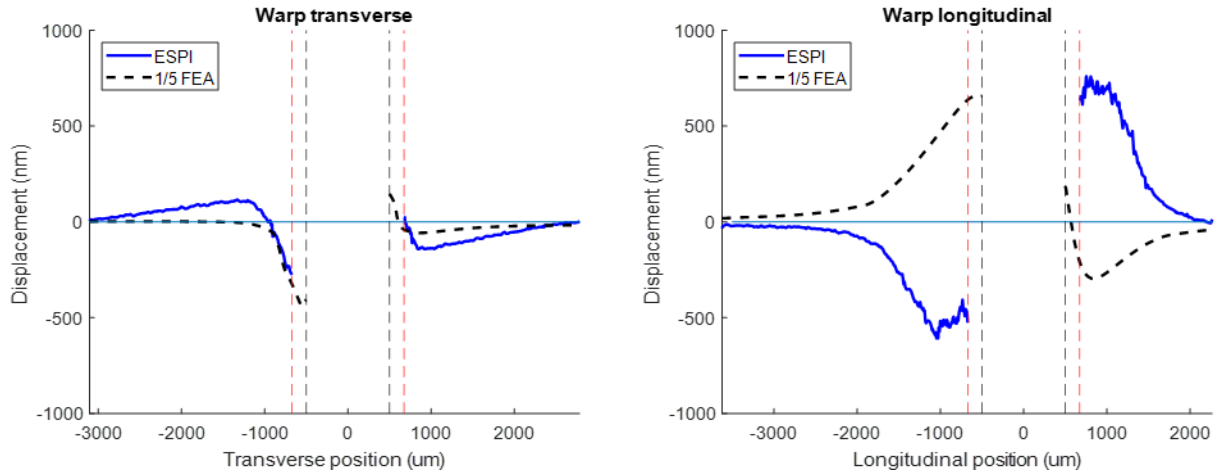
Figure 15: Slices through the displacement fields of Figure 14. The red dashed line shows the region of the experimental data that was excluded. The black dashed data line is the FEA prediction divided by 5.

4.1.4 Orthogonal weft results

The results for the hole in the orthogonal weft tow are shown in Figure 16. Both the experiment and the prediction show opening transverse to the tow. the shape of the transverse fields is very similar and a sharp change in displacement can be seen at similar distances from the hole in the surface displacement plots. The longitudinal experimental results and the prediction both show the hole closing along the length of the tow and the shape of the displacement fields are a strong match.
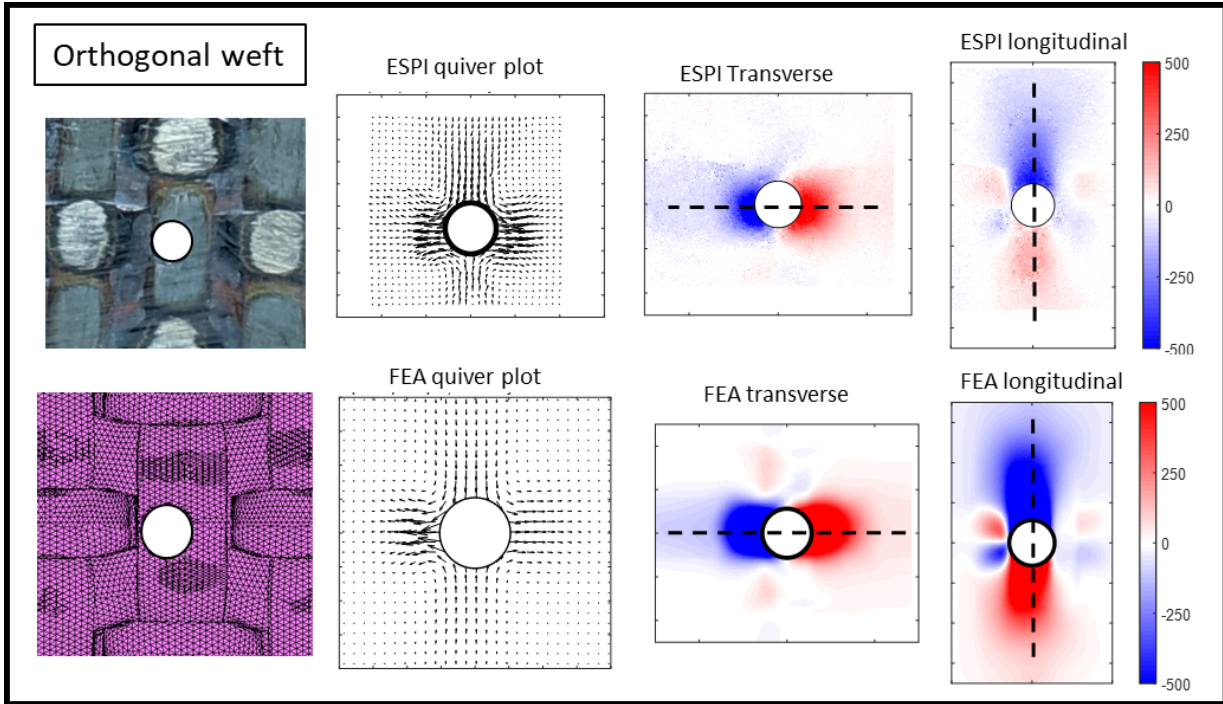
Figure 16: Observed (upper row) and predicted (lower row) displacement fields resulting from hole in the middle of the weft tow in the orthogonal structure. The dashed lines show the location and direction of the slice plots in Figure 17.

Figure 17 shows the slice plots for the hole in the weft tow from the Figure 16 data. Note that both plots use 1/5th of the predicted value. This better shows how the experimental results are approximately 1/5th of the prediction scale transverse to the tow. The longitudinal slices also exhibit the best correlation with 1/5th of the predicted results.
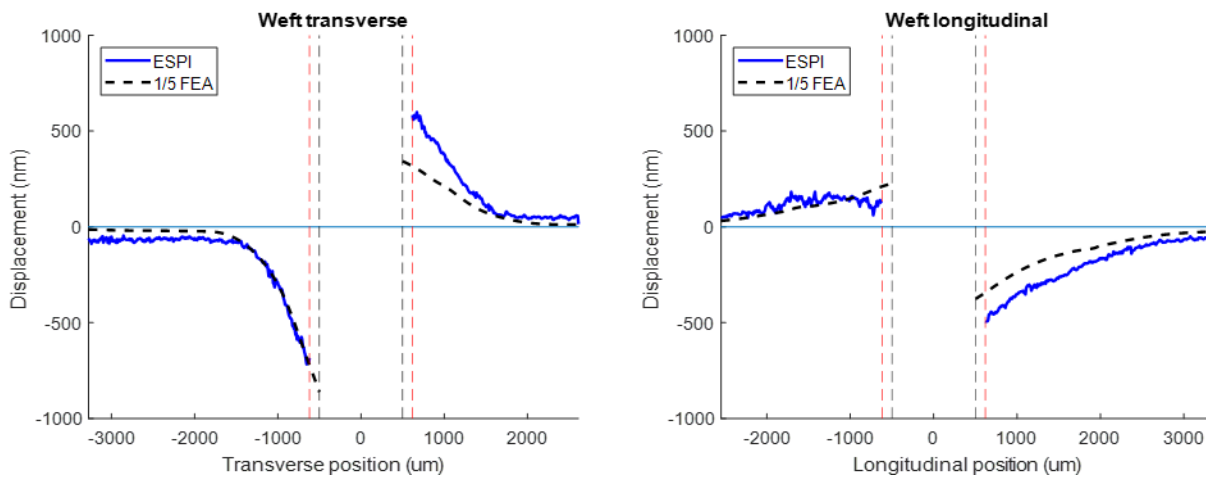
Figure 17: Slice plots for data shown in Figure 16. Both plots show good agreement with the FEA predictions divided by 5.

Almost all of the displacements in the orthogonal architecture are ~1/5th of the predicted values.

We attribute this to the extensive cracking in the resin pockets of the orthogonal weave relieving

the intrinsic residual stress which is not reflected in the model. The cross sectional image in

Figure 18 of the orthogonal composite shows major cracking in the resin pockets beneath the

through-the-thickness binder weave.
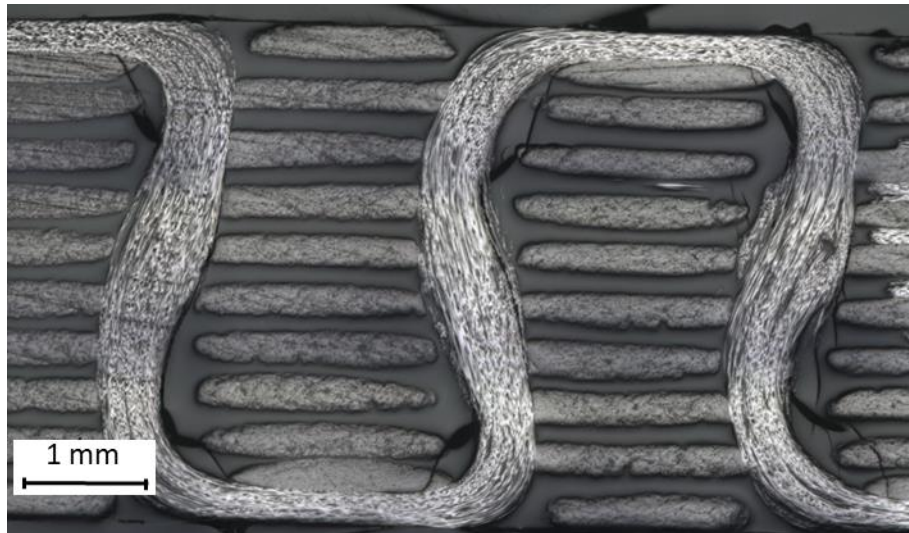
Figure 18: Cross section of Orthogonal weave showing cracks beneath the binder tow

The location of the hole has a significant impact on the displacement field. Figure 19 compares

the predicted displacement fields for the hole in the middle of the warp tow in the orthogonal

structure to the displacements that more closely match the location of the experimental hole. The

shape of the experimental and predicted displacement fields match when the hole locations are

closely matched but the shape of the displacement fields are very different when the hole in the

prediction is not closely matched in location to the actual hole.
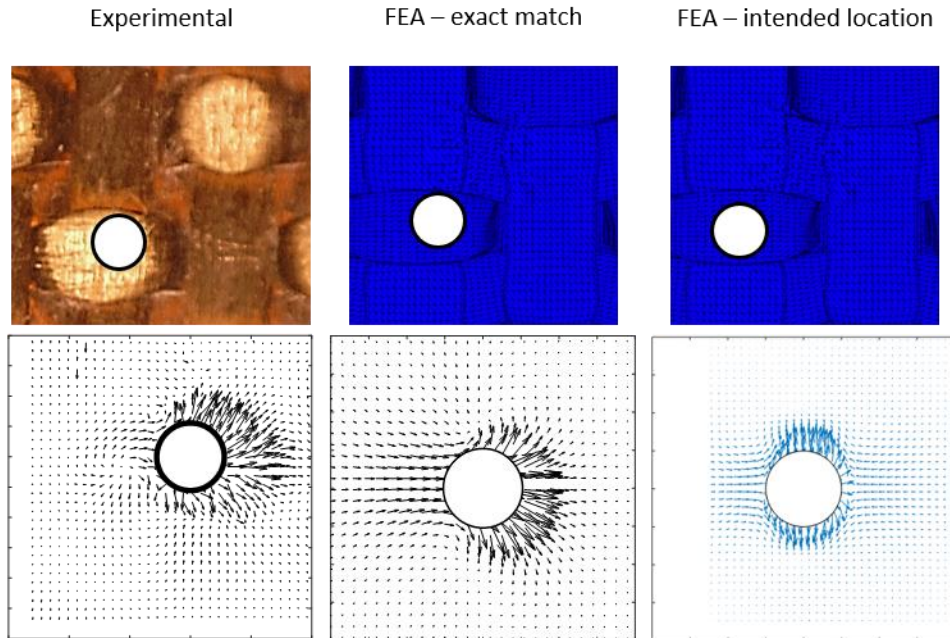
Figure 19: Observed displacement field for hole in warp tow compared to a precisely matched FE model hole location and symmetrically located FE model hole location. The symmetrical hole location predicts symmetrical, mostly transverse displacements. The displacement field for the accurate model location more closely resembles the observed field.

The experimental displacement field transverse to the ply-to-ply warp tow is a qualitative match to the predicted displacement and but the magnitude is between matching and two times larger than the predicted results. The predicted ply-to-ply weft hole displacement fields qualitatively match the experimental results both transverse to and parallel to the tow axis. The magnitude of the displacement fields is of a similar scale to the predicted results along the weft ply-to-ply tow, but is ~1/3rd to matching the magnitude transverse to the tow.

The experimental results for the orthogonal warp tow are ~1/5th the predicted displacement transverse to the warp tow and match in qualitative shape. Along the orthogonal warp tow the results are opposite sign, and the experimental displacement is approximately 1/5th of the predicted displacement. The experimental displacement is a good qualitative match but is ~1/5th the magnitude both along and transverse to the orthogonal weft tow axis.

Table 3 summarizes the observed qualitative and quantitative trends.

Table 3: Summary of qualitative and quantitative comparison of experimental observations and FEA predictions.

Hole location	Qualitative		Quantitative	
	Transverse to fiber axis	Along fiber axis	Transverse to fiber axis	Along fiber axis
Ply-to-ply warp	Match	Match	Match to 2x larger	One side match, one side 2x larger
ply-to-ply weft	Match	Match	1/3 to match	Match
Orthogonal warp	Similar	Opposite	1/3 to 1/5	-1/5
Orthogonal weft	Match	Match	1/5	1/5

4.2 Effect of drill depth on surface displacement in the orthogonal and 12x10 ppi ply-to-ply structures

The surface displacement fields were experimentally measured and predicted as a function of depth in 0.5 mm increments to determine the impact of the underlying tows on the surface displacement fields. The orthogonal weave is predicted, by the finite element model, to have the highest compressive stress along the warp tow axis as seen in Table 2. The stress relaxation of subsurface layers may be reflected on the surface of the composite depending on the magnitude of the stress. The ply-to-ply weave is expected to have less effect from drill depth due to the small magnitude predicted stresses in the sub-surface tows. The holes in the depth study have all been drilled in a finite element model that does not have the resin overburden artifact.

4.2.1 Ply-to-ply warp results

In Figure 20, the experimental hole drilled in the ply-to-ply warp tow shows hole closing along the length of the tow which matches the predicted displacement. The scale of the displacements is the same. The experimental displacement results show very little displacement change with depth. The only noticeable change is on one side of the hole from the 0.5mm to the 1.0 mm drill depth the hole shows slightly more closing. This matches the predicted displacement results which show no impact from depth. This is expected because as seen in Figure 8 the layers cut are alternating warp and weft fibers. As the layers are cut, the transverse tensile stress cancels the longitudinal stress from the tow above and the same thing occurs for the tow below.

Transverse to the ply-to-ply warp tow, the experimental results show close to the hole there is opening and further away a closing response. This matches the predicted displacement results in shape and scale and the sign change occurs at the same distance away from the hole in both the

33

experiment and simulation. The experimental displacement results show no change with depth, and neither does the model, as expected for the ply-to-ply results based on the alternating stress states.
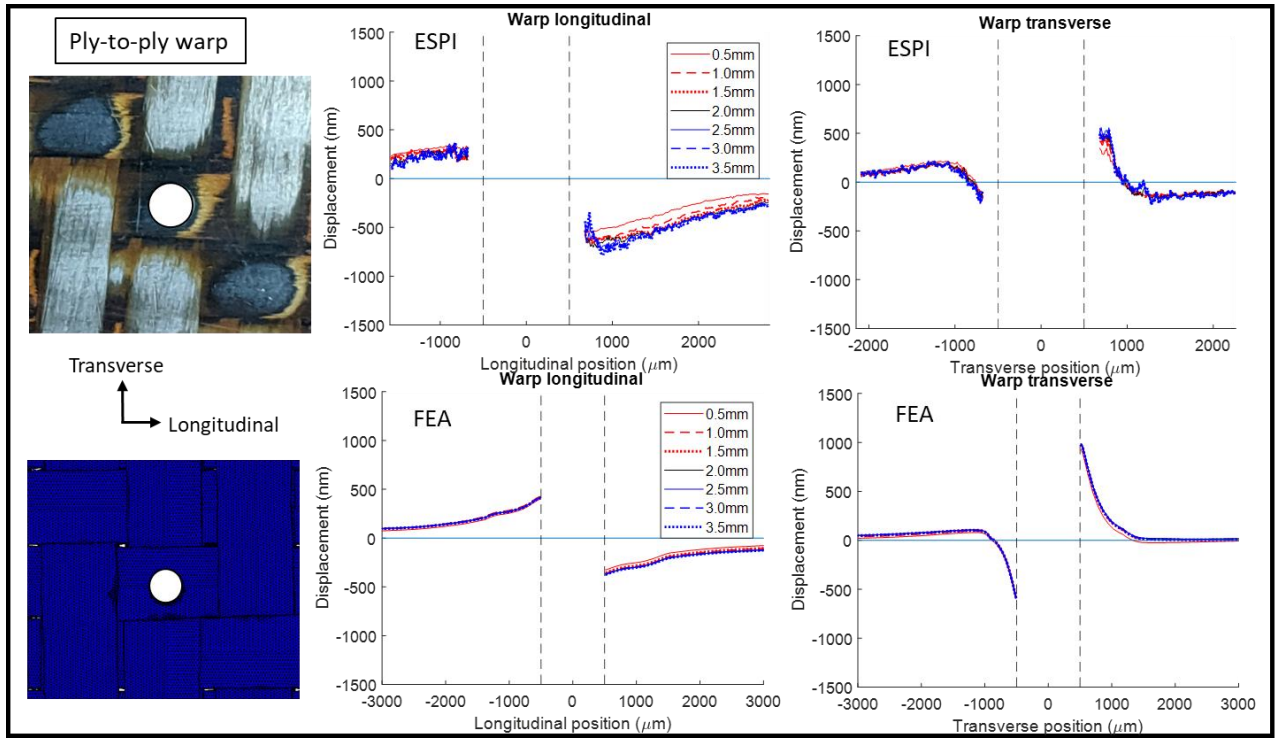
Figure 20: Predicted and experimental slice plots for hole drilled in the warp tow on the ply-to-ply structure. The top row shows the observed displacements and the bottom row shows the predicted displacements. The left hand images show the actual and predicted hole location. The middle figures show the displacement slices by depth along the length of the warp tow axis, in this case the horizontal direction. The right hand figures show the displacement slices by depth transverse to the warp tow axis, in this case the vertical direction.

4.2.2 Ply-to-ply weft results

In Figure 21, the ply-to-ply weft hole shows closing along the length of the fiber in the experimental results which matches the predicted results in shape and scale. There is no impact from depth in the experimental results and the simulation also shows no impact as expected based on the alternating stress layers shown in Figure 8.

Transverse to the ply-to-ply weft tow, the experimental results show hole opening which matches the predicted results and fits with the expected tension in the tow in the transverse direction. The experimental results show a very slight change with depth, but not enough to be significant. The predicted hole shows no change at all with depth.
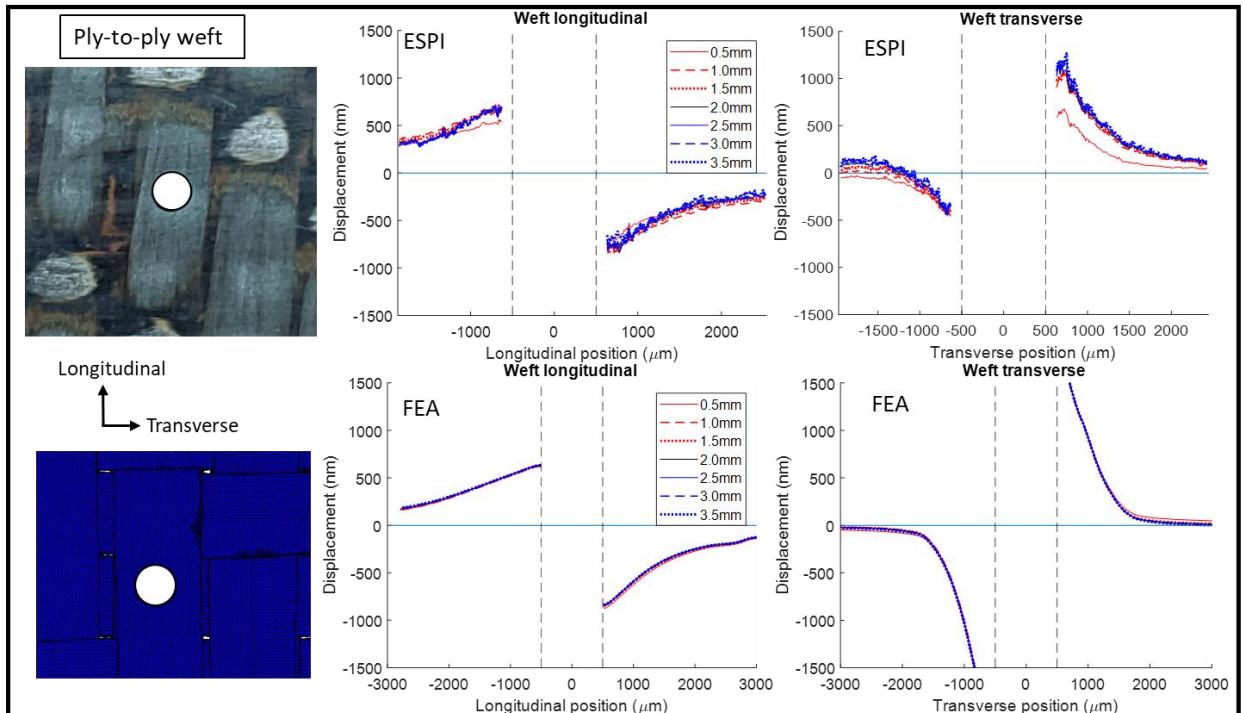
Figure 21: Predicted and experimental slice plots for hole drilled in the weft tow on the ply-to-ply structure. The top row shows the observed displacements and the bottom row shows the predicted displacements. The left hand images show the actual and predicted hole location. The middle figures show the displacement slices by depth along the length of the weft tow axis, in this case the vertical direction. The right hand figures show the displacement slices by depth transverse to the weft tow axis, in this case the horizontal direction.

4.2.3 Orthogonal warp results

In Figure 22, the orthogonal warp tow shows hole opening along the length of the tow in the experimental results. The predicted displacement shows the right side opening and the left side closing, which appears as the hole shifting to the right along the length of the tow. The experimental displacements on the right side of the hole match the predicted results, and as seen in Figure 22 the right edge of the hole is in a similar location in relation to the resin pockets and the weft tow below. However, on the left side where the experimental results do not match the prediction; the left edge of the hole is in a different location. In the experimental picture (top left image in Figure 22) the left edge of the hole is approximately lined up with the edge of the weft tow below, while the location of the left edge of the hole left edge in the model is almost centered over the weft tow below. The experimental displacement field shows the same impact from depth as the predicted displacement field. Figure 7 shows the in plane stresses in the orthogonal architecture and in the top left image the weft fibers throughout the depth of the weave are in tension transverse to the weft tow axis. So the displacements along the surface warp tow are expected to increasingly show opening as the weft tows below are cut and add to the opening displacements. The experimental displacement field matches this prediction and the finite element slice plot in the right side matches. The left side shows the displacements decreasing with increasing depth, representing released tension with depth, matching the expected tension in the weft tows below.

Transverse to the warp tow, the experimental results show a very small local hole opening response and a far field closing which is the same result that the simulation. The second hole drilled, from 0.5mm to 1.0mm, shows an increase in displacement but no additional impact on

displacement with increasing depth in the experimental results. This is the same result that is seen in the prediction for the orthogonal warp hole. The increasing compressive displacement transverse to the warp tow with depth is expected based on compression along the length of the sub-surface weft tows beneath the warp tow as seen in Figure 7.
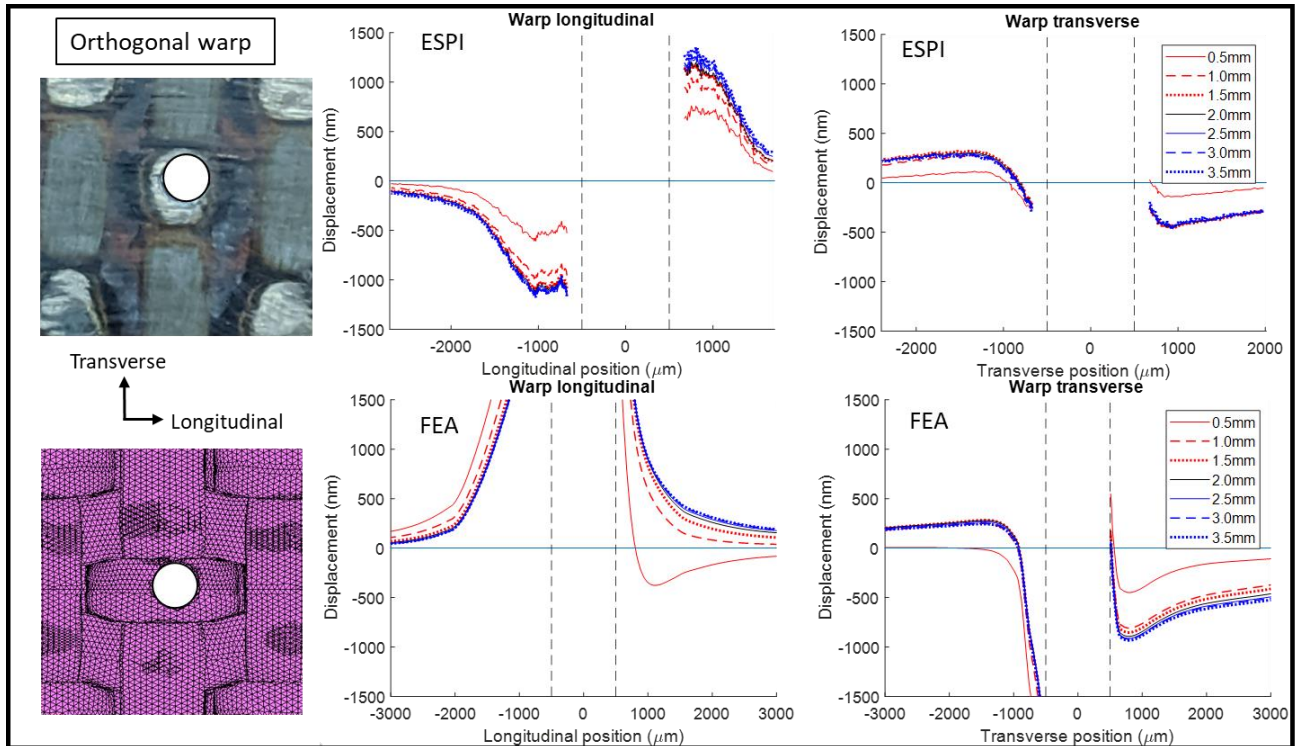
Figure 22: Predicted and experimental slice plots for hole drilled in the warp tow on the orthogonal structure. The top row shows the observed displacements and the bottom row shows the predicted displacements. The left hand images show the actual and predicted hole location. The middle figures show the displacement slices by depth along the length of the warp tow axis, in this case the horizontal direction. The right hand figures show the displacement slices by depth transverse to the warp tow axis, in this case the vertical direction.

4.2.4 Orthogonal weft results

In Figure 23, the orthogonal weft hole shows closing along the length of the tow. The prediction also shows closing; however, the magnitude of the predicted displacement is three times larger. The experimental displacement shows no impact from depth which matches the trend for the predicted displacement.

Transverse to the orthogonal weft hole the experimental results show the hole opening consistent with a tensile stress. This matches the predicted hole displacement in shape and magnitude. Figure 7 shows the finite element prediction of in-plane stress and, since the weft tows below the surface are in transverse tension, it is expected that the displacements transverse to the weft tow will continue to increase with depth. The experimental result shows a small impact from depth, most noticeably from the 0.5mm drill depth to the 1.0 mm depth. This jump matches the one seen in the predicted displacements. A slight depth impact at each step after the 1.0mm depth is seen in the experimental and predicted displacements.
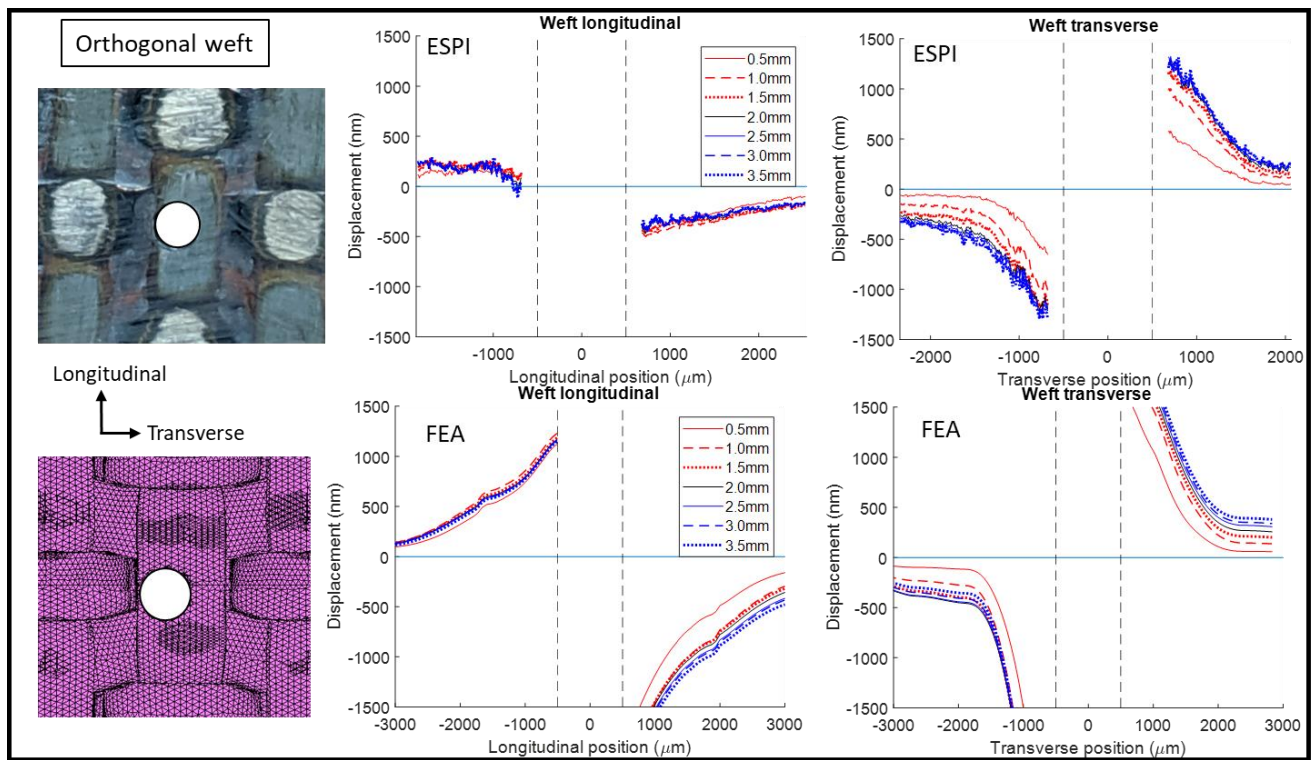
Figure 23: Predicted and experimental slice plots for hole drilled in the weft tow on the orthogonal structure. The top row shows the observed displacements and the bottom row shows the predicted displacements. The left hand images show the actual and predicted hole location. The middle figures show the displacement slices by depth along the length of the weft tow axis, in this case the vertical direction. The right hand figures show the displacement slices by depth transverse to the weft tow axis, in this case the horizontal direction.

4.2.5 Summary

Table 4: Summary of depth study results

Hole location	Qualitative comparison		Depth impact comparison	
	Transverse to fiber axis	Along fiber axis	Transverse to fiber axis	Along fiber axis
001 warp	Match	Match	Match	Match
001 weft	Match	Match	Match	Match
008 warp	Match	One side match	Match	Match
008 weft	Match	Similar	Match	Similar

4.3 Effect of pick spacing and volume fraction on apparent residual stress

We studied four variations of ply-to-ply structures that have little or no internal cracking to further evaluate the accuracy of the finite element model predictions. The weaves chosen were 12x12 picks-per-inch (ppi), 10x12 ppi, and 10x8 ppi, which results in different warp, weft, and overall volume fraction of tows, listed in Table 1. The drill depth was selected to be 0.3 mm deep to only cut through the first tow layer but not the second.

Table 5: Comparison of displacements obtained experimentally and through finite element models for a 12x10 ply-to-ply warp tow. The third column is the predicted displacement in a model that has removed the resin overburden artifact. The fourth column is the displacement obtained through the original model with the resin overburden.

Ply-to-ply Warp	Experimental displacement	Predicted displacement (no resin)	Predicted displacement (resin overburden)
Hole Location			
Longitudinal			
Transverse			
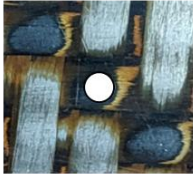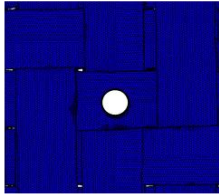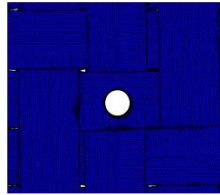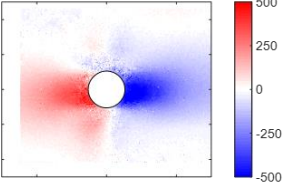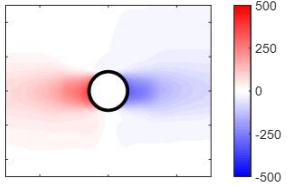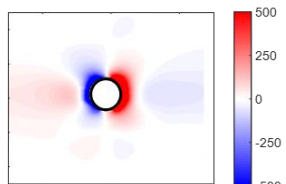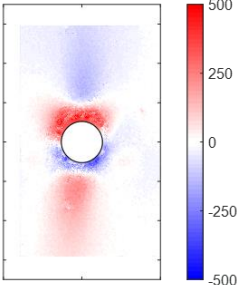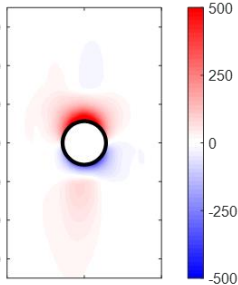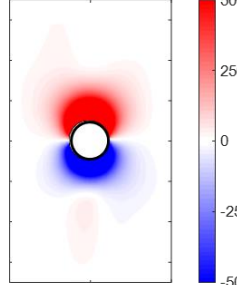
The simulation results shown in this section predict outward displacements very near to the edge of the hole along the tow axis that change sign from the far field inward displacements. This is attributed to a resin overburden on top of the tow in the model which is under tensile stress. A new model without the epoxy overburden was constructed for the orthogonal and ply-to-ply weaves that does not predict the near hole outward displacements, confirming this effect is due to the epoxy overburden in the model. Table 5 compares the experimental results for a hole drilled in the12x10 ply-to-ply warp tow. The experimental displacement field and the predicted field with no resin overburden are a match whereas the predicted field with the resin overburden has the strong local effect. The experimental results presented in this section are accurate but the alternative weave models that do not have the epoxy overburden have not yet been recreated at the time of the writing of this thesis.

4.3.1 Warp results

The predicted displacement along the tow axis of the warp holes show a local opening around the hole and a far field closing response. This local response is not observed in the experimental results and is attributed to the inclusion of the resin overburden in the FE model. The slice plots seen in Figure 24, Figure 25, and Figure 26 show that the experimental displacement signs match the predicted displacements and the shape of the curve is similar.

The difference in magnitude between the predicted and observed displacements along the tow axis of the warp hole increases as the number of picks-per-inch decreases. The magnitude of the experimental displacements for 12x12 ppi matches the predicted displacement. The magnitude of the experimental displacements for the 10x12 ppi structure is approximately 1/2 of the predicted displacements. The magnitude of the experimental displacements for the 10x8 ppi structure is 4-8x greater displacement than predicted, and is ~2x larger than the other experimental warp tow displacements.
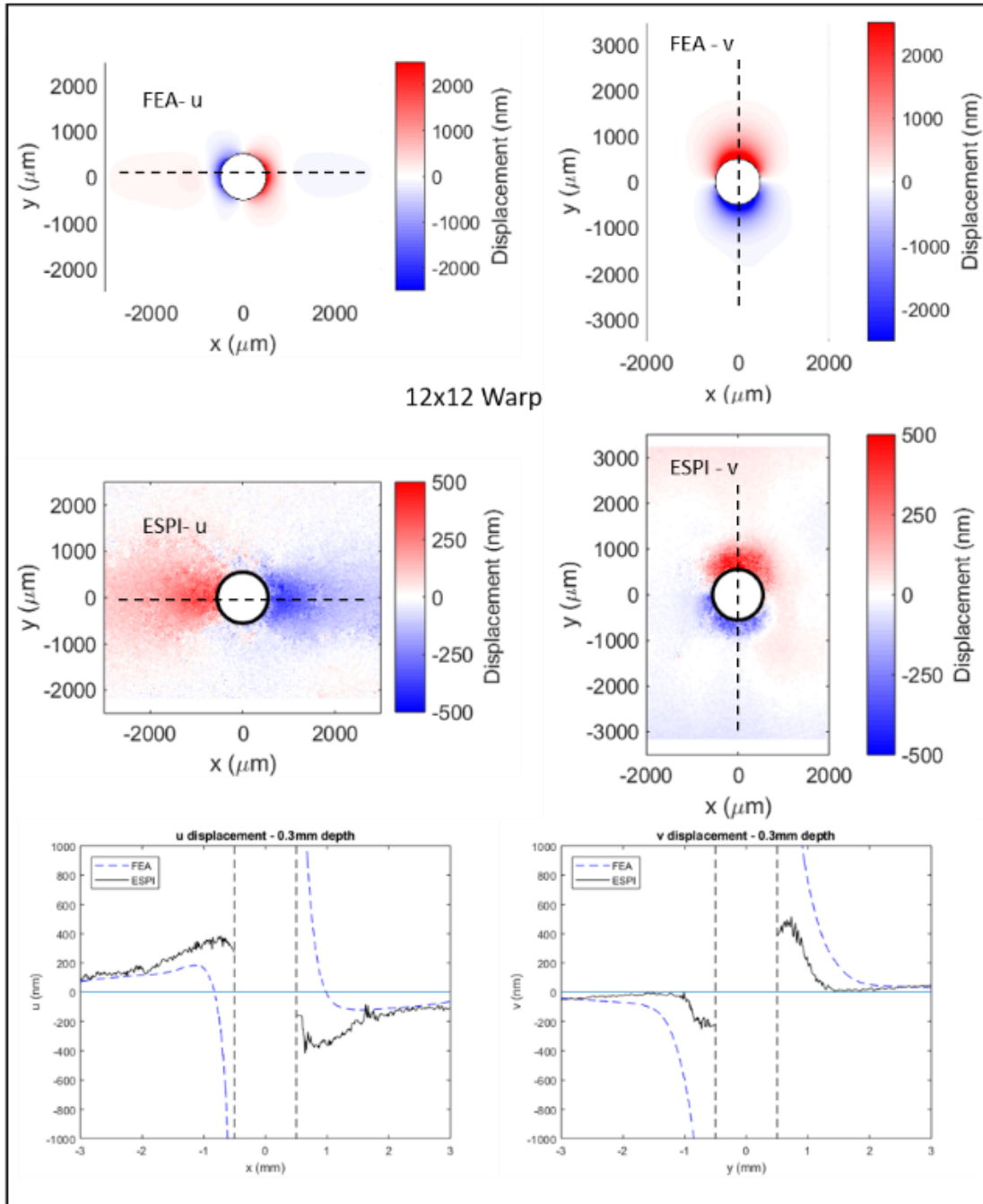
Figure 24: Predicted and experimental displacement fields and slice plots for hole drilled in warp tow on 12x12 ppi structure. The u displacements are horizontal and in the warp direction. The v displacements are in the vertical direction and transverse to the tow. Note that the displacement scale for the FE results is 5 times that for the experimental results.

43
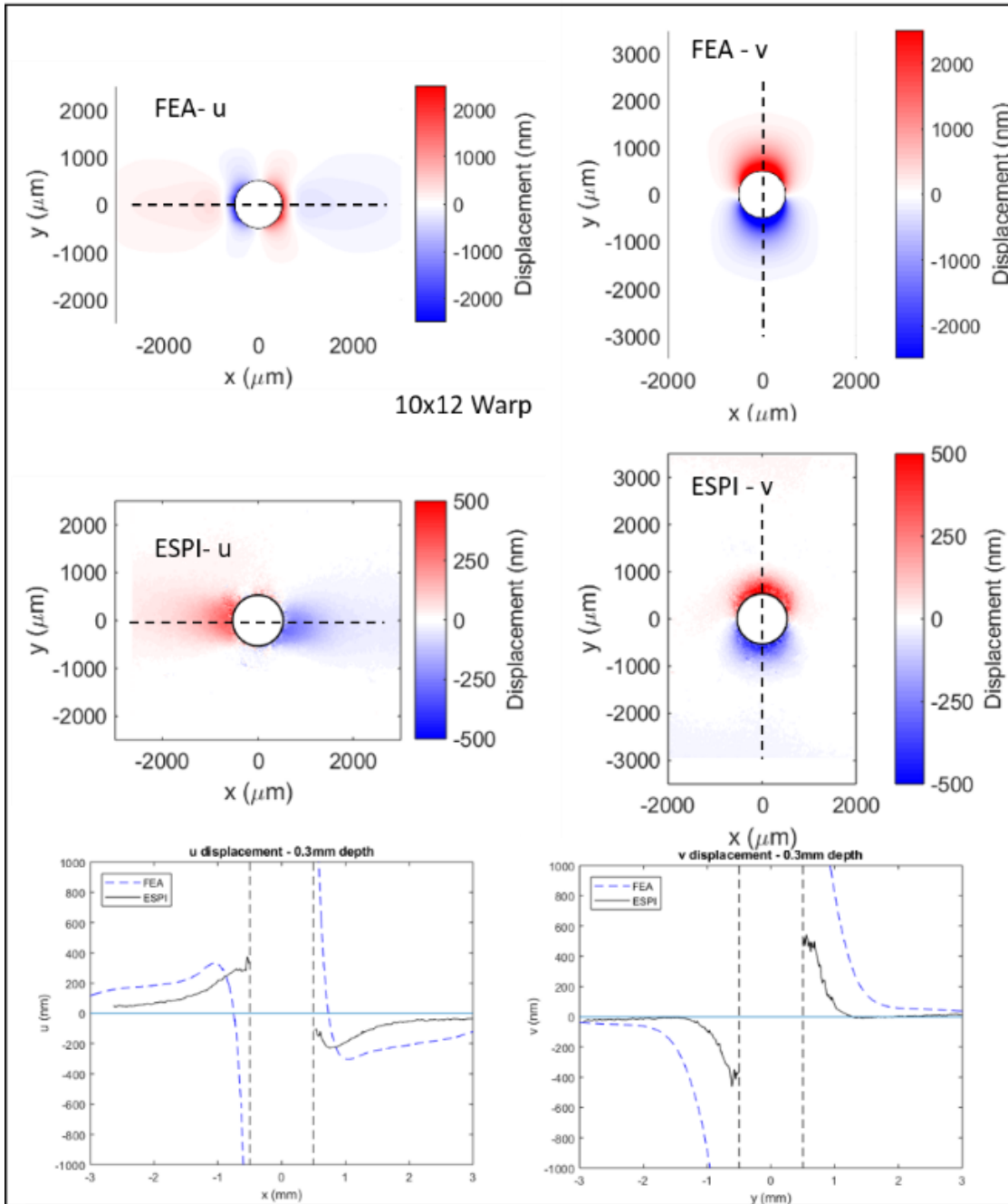
Figure 25: Predicted and experimental displacement fields and slice plots for hole drilled in warp tow on 10x12 ppi structure. The u displacements are horizontal and in the warp direction. The v displacements are in the vertical direction and transverse to the tow. Note that the displacement scale for the FE results is 5 times that for the experimental results.
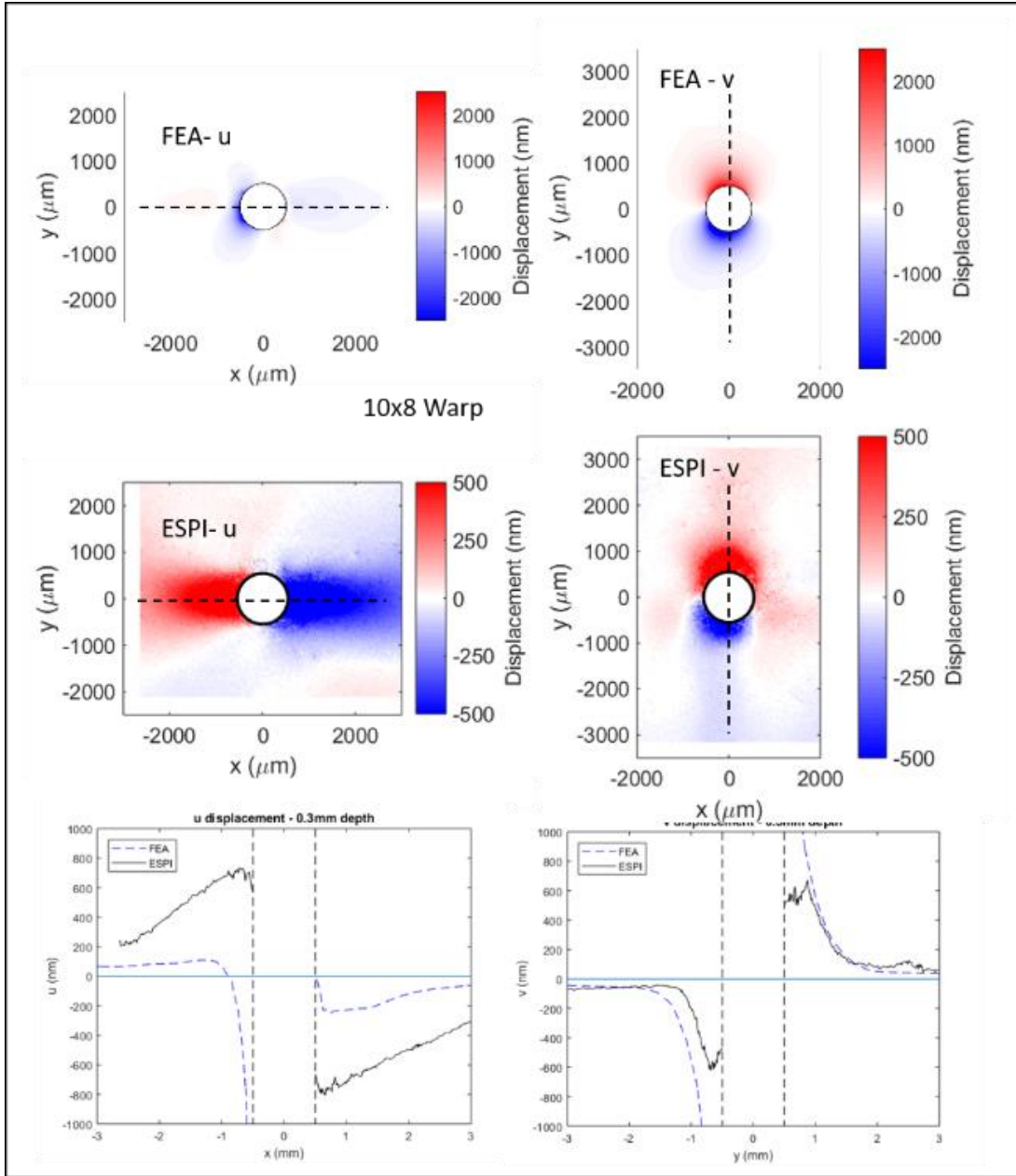
Figure 26: Predicted and experimental displacement fields and slice plots for hole drilled in warp tow on 10x8 ppi structure. The u displacements are horizontal and in the warp direction. The v displacements are in the vertical direction and transverse to the tow. Note that the displacement scale for the FE results is 5 times that for the experimental results.

4.3.2 Weft results

The observed displacements along the weft tow axis show a far field closing response which is consistent with the predicted displacement along the warp tow axis. The experimental displacements reflect the far field closing response as seen in Figure 27, Figure 28, and Figure 29. The predictions of near-hole opening response attributed to the local resin overburden can be seen in the predicted displacements in these figures.

The observed displacement field for the 10x12 ppi along the weft tow is the most similar to the predicted displacement field. The 12x12 ppi observed displacement fields along the weft tow are a good match to the predicted far field results. The observed displacement field along the weft tow in the 10x8 ppi structure is 4-8x larger than the predicted displacement in the far field, which is the same as for the 10x8 displacement field along the warp tow.

The observed displacement fields transverse to the weft tow axis' show a good qualitative match with the predicted displacement fields. The displacement fields show opening transverse to the tow axis' which matches the previously mentioned trend in the ply-to-ply and orthogonal weaves. The slice plots show a similar decrease in displacement with radius between observed and predicted displacements. The magnitude of the experimental displacement is ~1/4 of the predicted displacement for all weft transverse hole results. This is the same as the results for the warp transverse holes.
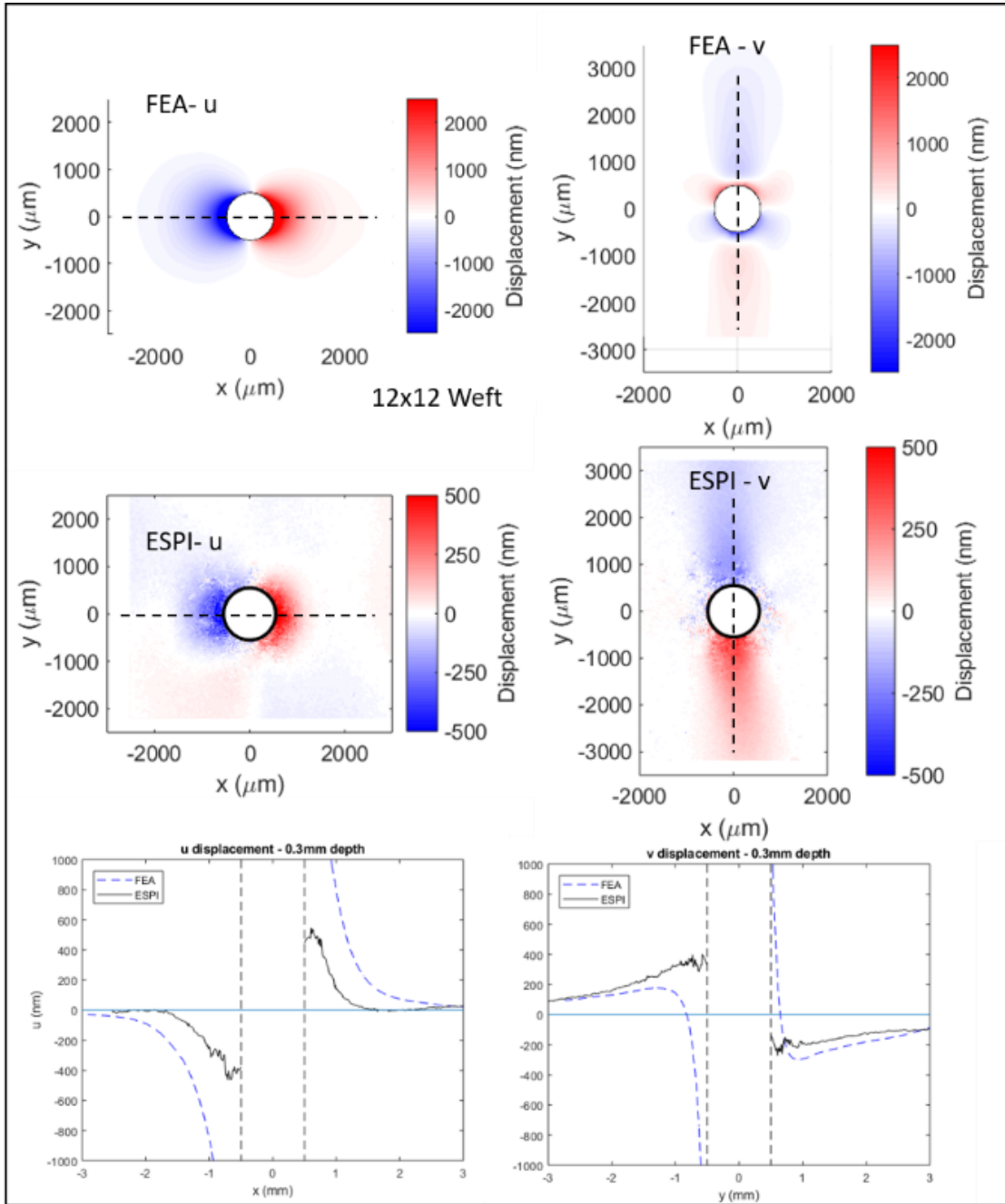
Figure 27: Predicted and experimental displacement fields and slice plots for hole drilled in weft tow on 12x12 ppi structure. The u displacements are horizontal and in the warp direction. The v displacements are in the vertical direction and transverse to the tow. Note that the displacement scale for the FE results is 5 times that for the experimental results.
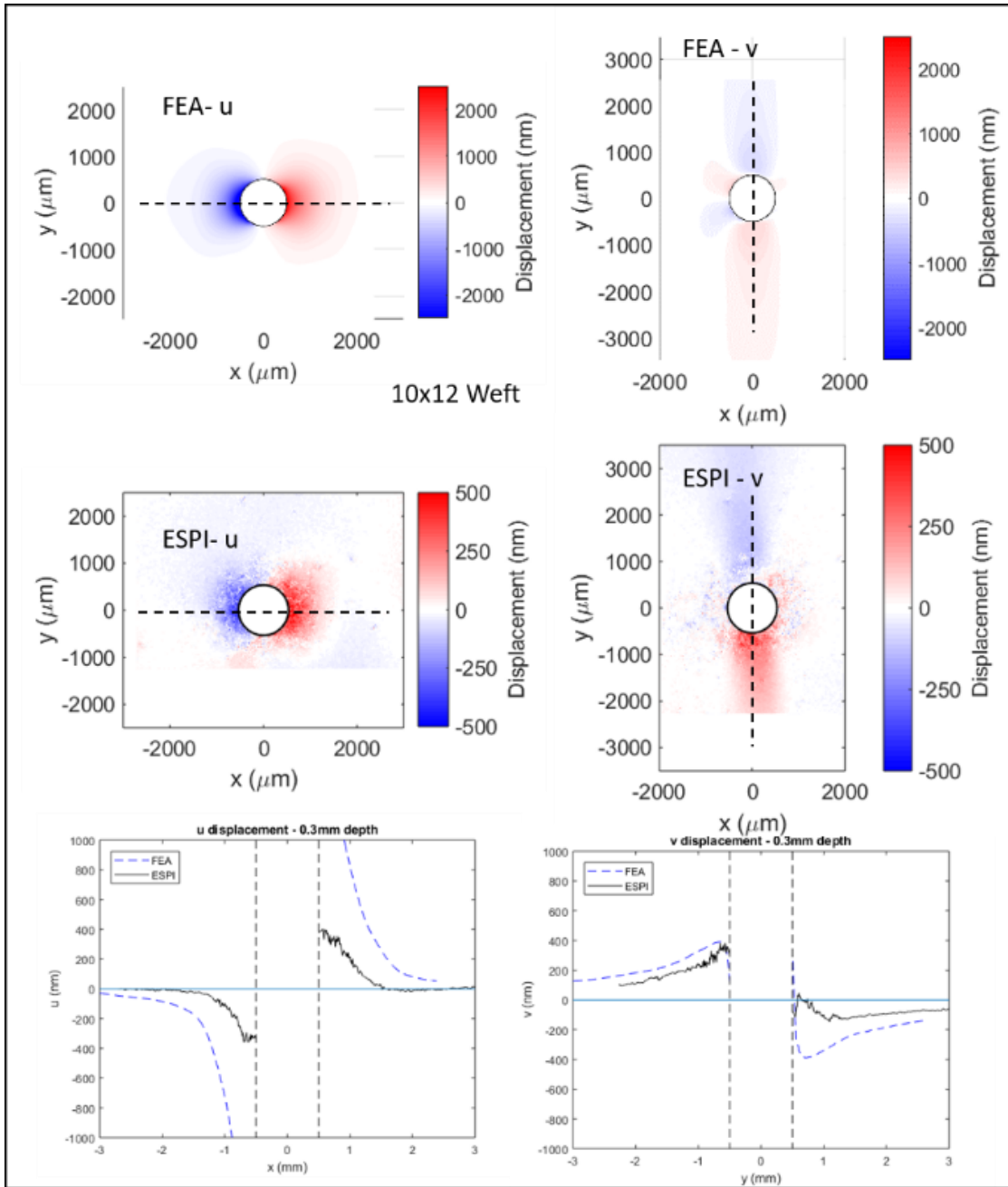
Figure 28: Predicted and experimental displacement fields and slice plots for hole drilled in weft tow on 10x12 ppi structure. The u displacements are horizontal and in the warp direction. The v displacements are in the vertical direction and transverse to the tow. Note that the displacement scale for the FE results is 5 times that for the experimental results.
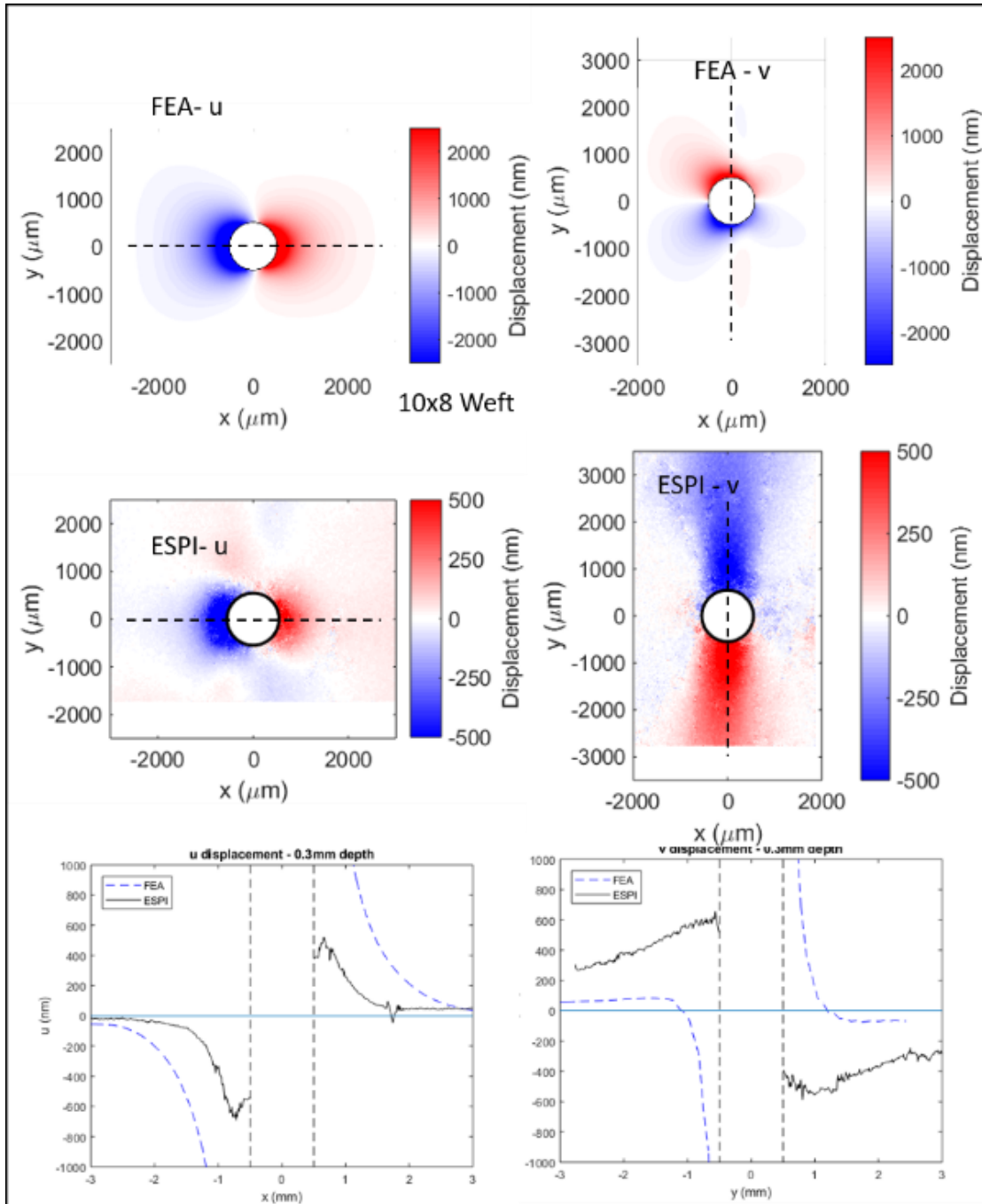
Figure 29: Predicted and experimental displacement fields and slice plots for hole drilled in weft tow on 10x8 ppi structure. The u displacements are horizontal and in the warp direction. The v displacements are in the vertical direction and transverse to the tow. Note that the displacement scale for the FE results is 5 times that for the experimental results.

4.3.3 Summary

*Table 6: Alternate weave study results. Note the local field qualitative mismatch due to the model resin overburden. The quantitative numbers represent the scale difference between experiment and simulation. The simulation results * the quantitative scale = the experimental result.*

Hole location	Qualitative		Quantitative	
	Transverse to fiber axis	Along fiber axis	Transverse to fiber axis	Along fiber axis
12x12 warp	Match	Local opposite, far field match	1/4	Match
12x12 weft	Match	Local opposite, far field match	1/4	Match
10x12 warp	Match	Local opposite, far field match	1/4	1/2
10x12 weft	Match	Local opposite, far field match	1/4	Almost match
10x8 warp	Match	Local opposite, far field match	Match	4-8x larger
10x8 weft	Match	Local opposite, far field match	1/4	4-8x larger

Chapter 5: Summary and Conclusions

The goal of this study was to experimentally evaluate the accuracy of finite element predictions of intrinsic residual stress in 3D woven composites using hole drilling as a method to detect the residual stress. The predictions were tested in three scenarios. First the experimental results of orthogonal and ply-to-ply architectures are compared to finite element models for holes that where drilled through the top tow and part of the tow below. Second, the alternate weave study evaluated the effect of weave density on the results and the model accuracy. And third is the hole depth study, investigating how the through-the-thickness binder weave affects the surface displacements and the model's ability to capture that effect.

The first goal was to compare the experimental results to the predicted finite element model results for two weave architectures; one with high through-thickness constraint (orthogonal) and the other with low through-thickness constraint (12x10 ply-to-ply). Along the tow axis in the ply-to-ply material, the observed displacements were between matching and two times larger than the predicted results. The observed displacements transverse to the tow axis in the ply-to-ply structure were between $1/3^{rd}$ to two times larger than the predicted displacements. The experimental ply-to-ply displacement fields were a qualitative match to the predicted displacement fields. Therefore, the model accurately predicts the form of the experimental response but not the scale. The observed displacements parallel to and transverse to the warp and weft tow axis in the orthogonal structure were all approximately $1/5^{th}$ the predicted displacements. The displacement field for the hole in orthogonal warp tow was similar to the predicted field transverse to the tow axis but the fields were of opposite sign along the tow axis. The experimental shape of the displacement field for the orthogonal weft tow matched the

predicted shape both along and transverse to the tow axis. The micro cracks observed relieve the out of plane stresses and this is mostly reflected in the binder tow response going from a prediction of compressive to tensile because the cracks allow the out of plane stress to be expressed. The cracks do not have as much of an effect on the weft tows because they are not oriented so that they would be strongly influenced by the out of plane stress.

The surface displacement fields were experimentally measured in the depth study as a function of depth in 0.5 mm increments to determine the impact of the underlying tows on the displacement fields in the orthogonal and ply-to-ply architectures. The resulting displacement fields and changes in field with depth are compared to the finite element model predictions. In the ply-to-ply architecture the displacement shows almost no change with depth and is extremely well matched to the finite element model prediction. The orthogonal architecture exhibits small experimental surface displacement changes for the first three, 0.5 mm drill steps, and the model also shows this small depth dependency. The ply-to-ply weave shows less depth dependency most likely due to the symmetric sub-surface weaves. The orthogonal architecture has only weft tows running under the surface warp tow, so the effect of cutting deeper is cumulative with no counter stresses to reduce the effect on surface displacement.

The alternate weave study was performed to investigate the effect of weave density on residual stress and to further test the models predictive capabilities for weaves with lesser through-thickness constraint. The woven panels had dimensions of 12x12, 10x12, and 10x8 picks per inch. For all holes, the shape of the experimental displacement fields transverse to the tow axis matched to the predicted displacement field. For all but one hole, the magnitude of the

experimental transverse displacement was 4-5x lower than the predicted. This strongly suggests that the stresses in the tow are relieved by inelastic deformation of the matrix in the tow during cooling. The predicted shapes of the displacement fields along the tow axis all had a near-hole region that suggested local tensile stresses instead of the expected compressive stresses exhibited by the far-field displacements. This is attributed to local relaxation of the thicker resin overburden in the model that was not present in the specimen. Subsequent models that did not have the resin overburden did not have the near-hole opening displacements. The magnitude of the far field displacement was roughly a match for the 12x12 and 10x12 ppi architectures. The 10x8 ppi experimental result was approximately 4-8x larger than predicted. This shows that the model fails to capture the effects of weave density on residual stress, and overall fails to capture the expected scale of displacements. When comparing the weaves against each other in order of least to most experimental displacement observed, the order is 12x12, 10x12, then 10x8 ppi. The largest displacements are observed in the least dense weave.

References

[1] I. M. Daniel and O. Ishai, Engineering Mechanics of Composite Materials, Oxford University Press, 1994, pp. 5-9.

[2] R. F. Gibson, Principles of Composite Material Mechanics, 3rd ed., CRC press, 2012, pp. 1-3.

[3] Y. Miao, E. Zhou, Y. Wang and B. Cheeseman, "Mechanics of textile composites:microgeometry," *Compos. Sci. Technol.,* vol. 68, pp. 1671-1678, 2008.

[4] Y. Wang and X. Sun, "Digital-element simulation of textile processes," *Compos. Sci. Technol.,* vol. 61, pp. 311-319, 2001.

[5] R. M. Jones, Mechanics of Composite Materials, 2 ed., Taylor & Francis, 1999, p. 26.

[6] H. Jafari, "INVESTIGATION ON EPOXY RESIN YIELDING UNDER PURE HYDROSTATIC STRESSES AND A NOVEL METHOD TO REDUCE MICROCRACKING," 2010.

[7] S. R. White and H. T. Hahn, "Process Modeling of Composite Materials: Residual Stress Development during Cure. Part I. Model Formulation".

[8] S. R. White and H. T. Hahn, "Process Modeling of Composite Materials: Residual Stress Development during Cure. Part II. Experimental Validation".

[9] G. Garschke, C. Weimer, P. Parlevliet and B. Fox, "Out-of-autoclave cure cycle study of a resin film infusion process using in situ process monitoring," *Composites Part A: Applied Science and Manufacturing,* vol. 43, no. 6, pp. 935-944, 2012.

[10] "HexFlow ® RTM6," 2018.

[11] H. M. El-Dessouky and M. N. Saleh, "3D Woven Composites: From Weaving to Manufacturing," in *Recent Developments in the Field of Carbon Fibers*, InTech, 2018.

[12] B. Drach, I. Tsukrov, A. Trofimov, T. Gross and A. Drach, "Comparison of stress-based failure criteria for prediction of curing induced damage in 3D woven composites," *Compos. Struct.* , vol. 189, 2018.

[13] S. R. Sobuj, "Motion of loom," 2015. [Online]. Available: https://textilestudycenter.com/motion-of-loom/.

[14] H. G. Da Silva and B. Drach, "Applicability of two-step homogenization in high-crimp woven composites," in *33rd Technical Conference of the American Society for Composites 2018*, 2018.

[15] F. V. Díaz, G. Kaufmann and G. Galizzi, "Determination of Residual Stresses Using Hole Drilling and Digital Speckle Pattern Interferometry with Automated Data Analysis," *Optics and Lasers in Engineering,* vol. 33, pp. 39-48, 10 2000.

[16] D. C. Ghiglia and L. A. (. N. L. Romero Albuquerque New Mexico 87185 (United States)), "Robust two-dimensional weighted and unweighted phase unwrapping that uses fast transforms and iterative methods," 1994.

[17] A. Drach, B. Drach and I. Tsukrov, "Processing of fiber architecture data for finite element modeling of 3D woven composites Dedicated to Professor Zdeněk Bittnar in occasion of his 70th birthday.," *Advances in Engineering Software,* 2014.

[18] B. Drach, A. Drach and I. Tsukrov, "Prediction of the effective elastic moduli of materials with irregularly-shaped pores based on the pore projected areas," *International Journal of Solids and Structures,* vol. 51, pp. 2687-2695, 10 2014.

[19] Z. Hashin, "Analysis of properties of fiber composites with anisotropic constituents," *J. Appl. Mech.,* vol. 46, pp. 543-550, 1979.

[20] R. Schapery, "Thermal expansion coefficients of composite materials based on energy principles," *J. Compos. Mater.,* vol. 2, pp. 380-404, 1968.

[21] L. F. Wu, J. G. Zhu and H. M. Xie, "Investigation of residual stress in 2D plane weave aramid fibre composite plates using moiré interferometry and hole-drilling technique," *Strain,* vol. 51, no. 6, pp. 429-443, 1 12 2015.

[22] H. G. M. G. J. G. T. F. M. M. L. Tsukrov Igor and Bayraktar, "Finite Element Modeling to Predict Cure-Induced Microcracking in Three-Dimensional Woven Composites," *International Journal of Fracture,* vol. 172, no. 2, pp. 209-216, 12 2011.

[23] I. Tsukrov, A. Drach, B. Drach, H. Bayraktar, J. Goering and T. Gross, "Numerical predictions of damage initiation in 3D woven composites under various loading conditions," 2014.

[24] Y. L. Dong and B. Pan, "A Review of Speckle Pattern Fabrication and Assessment for Digital Image Correlation," *Experimental Mechanics,* vol. 57, no. 8, pp. 1161-1181, 1 10 2017.

[25] H. Bayraktar, I. Tsukrov, M. Giovinazzo, J. Goering, T. Gross, M. Fruscello and L. Martinsson, "Development of Realistic Simulation Techniques to Predict Cure-Induced Microcracking in 3D Woven Composites," *Collection of Technical Papers - AIAA/ASME/ASCE/AHS/ASC Structures, Structural Dynamics and Materials Conference,* p. , 10 2011.

[26] S. Akbari, F. Taheri-Behrooz and M. M. Shokrieh, "Characterization of residual stresses in a thin-walled filament wound carbon/epoxy ring using incremental hole drilling method," *Composites Science and Technology,* vol. 94, pp. 8-15, 9 4 2014.